

1 **Coupled Mesoscale-Large-Eddy Modeling of Realistic Stable Boundary Layer**
2 **Turbulence**

3 Yao Wang,¹ Sukanta Basu,^{1, a)} and Lance Manuel²

4 ¹⁾*Department of Marine, Earth, and Atmospheric Sciences,*
5 *North Carolina State University, Raleigh, NC 27695*

6 ²⁾*Department of Civil, Architectural and Environmental Engineering,*
7 *University of Texas, Austin, USA*

8 (Dated: 8 July 2013)

Site-specific flow and turbulence information are needed for various practical applications, ranging from aerodynamic/aeroelastic modeling for wind turbine design to optical diffraction calculations. Even though highly desirable, collecting on-site meteorological measurements can be an expensive, time-consuming, and sometimes a challenging task. In this work, we propose a coupled mesoscale-large-eddy modeling framework to synthetically generate site-specific flow and turbulence data. The workhorses behind our framework are a state-of-the-art, open-source atmospheric model called the Weather Research and Forecasting (WRF) model and a tuning-free large-eddy simulation (LES) model.

Using this coupled framework, we simulate a nighttime stable boundary layer (SBL) case from the well-known CASES-99 field campaign. One of the unique aspects of this work is the usage of a diverse range of observations for characterization and validation. The coupled models reproduce certain characteristics of observed low-level jets. They also capture various scaling regimes of energy spectra, including the so-called spectral gap. However, the coupled models are unable to capture the intermittent nature of the observed surface fluxes. Lastly, we document and discuss: (i) the tremendous spatio-temporal variabilities of observed and modeled SBL flow fields, and (ii) the significant disagreements among different observational platforms. Based on these results, we strongly recommend that future SBL modeling studies consider rigorous validation exercises based on multi-sensor/multi-platform datasets.

In summary, we believe that the numerical generation of realistic SBL is not an impossible task. Without any doubt, there remain several computational and fundamental challenges. The present work should be viewed as a first step to confront some of these challenges.

^{a)}Electronic mail: sukanta.basu@ncsu.edu

9 I. INTRODUCTION

10 Over the past two decades or so, several large-eddy simulation (LES) studies (e.g.,^{3,8,14,21,39,45,54,75,101})
11 were conducted to enhance our understanding of atmospheric stable boundary layers (SBLs).
12 Initially, some of these studies encountered various modeling challenges including, but not
13 limited to, unusual subgrid-scale (SGS) modeling behavior, excessive resolution sensitivity,
14 difficulty in initialization, unphysical runaway surface cooling, unexpected model crashing,
15 etc. With the advent of robust SGS models (e.g., various types of dynamic SGS models)
16 along with the easy availability of high-performance computing resources, the quality of SBL
17 simulations has improved substantially. Researchers are gaining more confidence in LES-
18 generated SBL data and have already started using them to complement sparsely available
19 observational data. For example, recently, an extensive LES database (called the NCSU-
20 LES database) of idealized SBLs has been utilized to address an age-old problem of stability
21 dependence of critical bulk Richardson number⁷³. Such LES studies are not only making
22 immense contributions to the fundamental science of SBLs, they are also impacting ap-
23 plied studies. For example, the NCSU-LES database has also helped researchers to identify
24 rotor-scale flow variables that influence extreme and fatigue loads on wind turbines⁶⁸.

25 One of the drawbacks of the aforementioned idealized LES studies is that they have
26 fallen short with regard to capturing ‘real-world’ SBL turbulence. This is due to the fact
27 that these simulations did not include: (i) the effects of natural topography and land-surface
28 heterogeneities, (ii) baroclinicity, large-scale advection, and subsidence effects, and (iii) in-
29 teractions among several physical processes—e.g., turbulence, radiative transfer, and cloud
30 microphysics. To partially fill this void, a handful of realistic LES studies were conducted
31 recently (e.g.,^{12,13,15,46}). These studies used site-specific observations to initialize and to
32 force their simulations. Encouraging results have been reported. For example, Basu et al.¹²
33 showed that a tuning-free LES model can reliably capture the development, magnitude, and
34 location of an observed nocturnal low-level jet (LLJ).

35 Due to a variety of logistical, financial, and instrumental issues, high-quality SBL data
36 are difficult to collect. So, from a practical standpoint, the initialization and forcing of an
37 LES model based on local observations has not been common. An alternative is to run a
38 mesoscale meteorological model (MMM) for a desired geographical region and time frame
39 and, then, to dynamically downscale the simulated fields using LES. In this study, we propose

40 a new coupled modeling framework to achieve this goal and demonstrate its strengths and
41 weaknesses.

42 The structure of this paper is as follows. In Section 2, we provide some background
43 on existing coupled modeling frameworks. Our proposed framework is discussed in Section
44 3. A case study and associated observational datasets are described in Sections 4 and 5,
45 respectively. Sections 6 and 7 provide detailed information on our modeling activities. A
46 wide range of observed and simulated statistics are discussed in Section 8. In that section,
47 we also document the results from several sensitivity experiments. Finally, in Section 9, we
48 summarize our findings and provide some concluding remarks.

49 II. BACKGROUND

50 Mesoscale meteorological models simulate or forecast atmospheric phenomena includ-
51 ing (but not limited to) convective clouds, thunderstorms, squall lines, frontal circulations,
52 low-level jets, terrain-induced mesoscale circulations, land-/sea-breezes, urban heat island
53 circulations, mountain-valley winds, lee waves, and gravity waves^{17,47}. The spatial and tem-
54 poral scales associated with these phenomena are on the order of $\approx 2 - 2000$ km and $1 - 48$
55 h, respectively^{17,47,67}. Over the past three decades, due to the increased availability of com-
56 putational resources, the overall performance of MMMs has been steadily increasing—grid
57 resolutions are getting finer; computational domain sizes are now larger; model physics pa-
58 rameterizations are becoming more complex; the number of ensemble members is growing;
59 etc. Most importantly, due to the enhanced capabilities of the MMMs, their application
60 arenas are also broadening. For example, even until only a decade ago, MMMs were rarely
61 used for commercial wind energy applications. Now, they represent a significant part of the
62 most common tools used by the wind industry (e.g.,²⁰). Another recent area of increased
63 application is in the field of laser propagation (e.g.,⁵²).

64 Despite their versatility, MMMs cannot be used to generate high-resolution, 4-D atmo-
65 spheric boundary layer (ABL) turbulence fields. This restriction is not due to any tech-
66 nological barriers; if anything, in the current era of petascale computing, one can utilize
67 thousands of processors and generate flow fields with a resolution of $O(10$ m). However, in
68 employing such brute-force computing, one violates two fundamental principles underlying
69 traditional mesoscale modeling. First, MMMs solve the Reynolds-Averaged Navier Stokes

70 (RANS) equations and, thus, the horizontal grid resolution of the MMMs must be larger
71 than the scale of the energy- and flux-containing turbulence⁹⁷. Since daytime ABL eddies
72 can be as large as several hundred meters, MMMs should not be run with sub-km reso-
73 lution. The second violation is related to the inherent assumption of most contemporary
74 MMMs—that turbulence mixing is dominated by vertical mixing. To be consistent with this
75 assumption, the aspect ratio of horizontal to vertical grid spacing near the surface should
76 be kept at a large value (see the discussion in¹⁰⁰). An aspect ratio of O(50:1) is common in
77 practice.

78 Given the difficulties of running MMMs with sub-km resolution, several coupled modeling
79 approaches have been proposed in recent studies^{49,51,59,74,76,90,98,99}. In all these approaches,
80 an MMM is either coupled with an engineering RANS model or with an LES model. These
81 approaches can be broadly classified into two: (i) one-way coupling; and (ii) two-way cou-
82 pling. Within the former class, several variants exist in the literature as is described below.
83 Please refer to⁷⁶ and⁹⁸ for other types of classification.

84 A. One-Way Coupling

85 In this approach, the information transfer is only one-way—from the MMM to the mi-
86 croscale model (MiM). This type of coupled modeling approach is relatively easy to im-
87 plement. It can be used to couple two separate models or to couple the same model with
88 different parameterizations for the MMMs and the MiMs. However, this approach faces two
89 fundamental issues. The first issue occurs when an engineering RANS model is used as an
90 MiM. From the literature, it is not clear whether grid resolutions utilized by the engineering
91 RANS models are always coarser than the energy-containing eddies. If they are not, one
92 again violates the RANS issue mentioned above. Since most of the engineering RANS mod-
93 els use 3-D diffusion, the aspect ratio issue mentioned above is not a problem. A different
94 issue arises when an LES model is used as an MiM. We know that an MMM generates an
95 ‘ensemble’ flow field, whereas an LES creates an ‘instantaneous’ field (which can be viewed
96 as one of the member of the ensemble). So, can we really prescribe MMM-simulated values
97 to run an LES? These issues need to be addressed in future research.

98 **1. Variant 1**

99 In this approach, a snapshot of the MMM run is used to provide the initial conditions for
100 the MiM. Then, the MiM (typically a RANS model) is run to reach a steady-state condition.
101 The MiM adjusts to the underlying fine-resolution topography or urban canopy during the
102 simulation. Schlünzen et al.⁷⁶ referred to this approach as a ‘time-slice approach’. Instead
103 of a single snapshot, multiple snapshots (available, say, every 3 h) from an MMM run can
104 also be used with this type of coupled approach.

105 **2. Variant 2**

106 In this coupled approach, the MMM provides both initial and continuous boundary con-
107 ditions to the MiM—an example is the simulation reported by Baik et al.⁵. They first
108 performed a mesoscale simulation using the MM5 model and stored the simulated results
109 every 10 min. Then, they linearly interpolated (in time and in vertical direction) the MM5
110 results to provide inflow and top boundary conditions to a RANS model. A qualitatively
111 similar approach was used by Talbot et al.⁹⁰. They coupled the Weather Research and
112 Forecasting (WRF) mesoscale model with the WRF-LES model.

113 **3. Variant 3**

114 This coupled approach is quite similar to Variant 2. Here, one uses a Newtonian relaxation
115 method (widely known as nudging in the meteorology literature) in addition to (or sometimes
116 in lieu of) lateral boundary conditions (e.g.,^{98,99}). This approach is highly sensitive to the
117 choice of the nudging coefficient (G). There is no universally accepted guidelines for the
118 specification of G . For example, Yamada and Koike⁹⁸ recommended G to be equal to
119 1% of the reciprocal of the integration time step. Thus, G is equal to 0.0001 s^{-1} and
120 0.01 s^{-1} , respectively, for typical MMM and MiM runs. In contrast, Zajackowski et al.⁹⁹
121 recommended that G be taken to be exactly equal to the reciprocal of the integration time
122 step (i.e., a factor of 100 different from the prescription by⁹⁸). The need to have an optimum
123 value of G is strongly emphasized by Schlünzen et al.⁷⁶.

124 The Variant 3 approach suffers from a more fundamental problem, which arises due
125 to the fact that the engineering MiMs usually do not contain important physics options

126 (e.g., buoyancy, radiation, microphysics). To illustrate, we briefly discuss a hypothetical
127 scenario, which is quite relevant to the present paper. Let us assume that a coupled MMM-
128 MiM approach with nudging option is being used to simulate a nocturnal stable boundary
129 layer. Furthermore, assume that the MiM does not contain a radiation parameterization.
130 The MMM generates a stable boundary layer which is deep due to the presence of both
131 turbulent and radiative flux divergences. Now, the MiM tries to capture this deep boundary
132 layer by (spuriously) generating excessive turbulent fluxes (since it is compensating for its
133 lack of radiation parameterization). In other words, the coupled approach would likely
134 generate physically unrealistic flow fields.

135 B. Two-Way Coupling

136 In this approach, the information transfer is two-way—from the MMM to the MiM and
137 vice versa. The information transfer from the MMM to the MiM is the same as in Variant
138 2 of the one-way coupling approach. In addition, the aggregated MiM results are used to
139 update the MMM results. Liu et al.⁵¹ demonstrated the strength of this approach in short-
140 term wind forecasting over complex terrain. It is possible that this approach suffers from
141 ‘double counting’ of diffusion⁹⁹. Based on our own research, we found that this approach
142 occasionally suffers from numerical instabilities. We also witnessed spurious flow patterns
143 at the nest boundaries. Similar problems were discussed in detail by Moeng⁶⁰.

144 III. PROPOSED MODELING FRAMEWORK

145 In order to avoid the unphysical influence of the MMM results on the MiM solutions, we
146 propose a different coupled modeling framework (see Fig. 1). In this approach, we extract
147 initial conditions, time-dependent lower-boundary conditions (e.g., near-surface air temper-
148 ature), and time-height-dependent large-scale forcings (e.g., geostrophic wind, mesoscale
149 advection of temperature) from the MMM output and utilize them for the LES runs.

150 We wish to point out that our proposed framework is conceptually similar to the one
151 recently reported by Rizza et al.⁷⁴. However, there are some technical differences; most
152 importantly, Rizza et al.⁷⁴ neglected the effects of mesoscale advection forcings in their study.
153 In the present work, we will demonstrate the importance of these forcings. Furthermore,

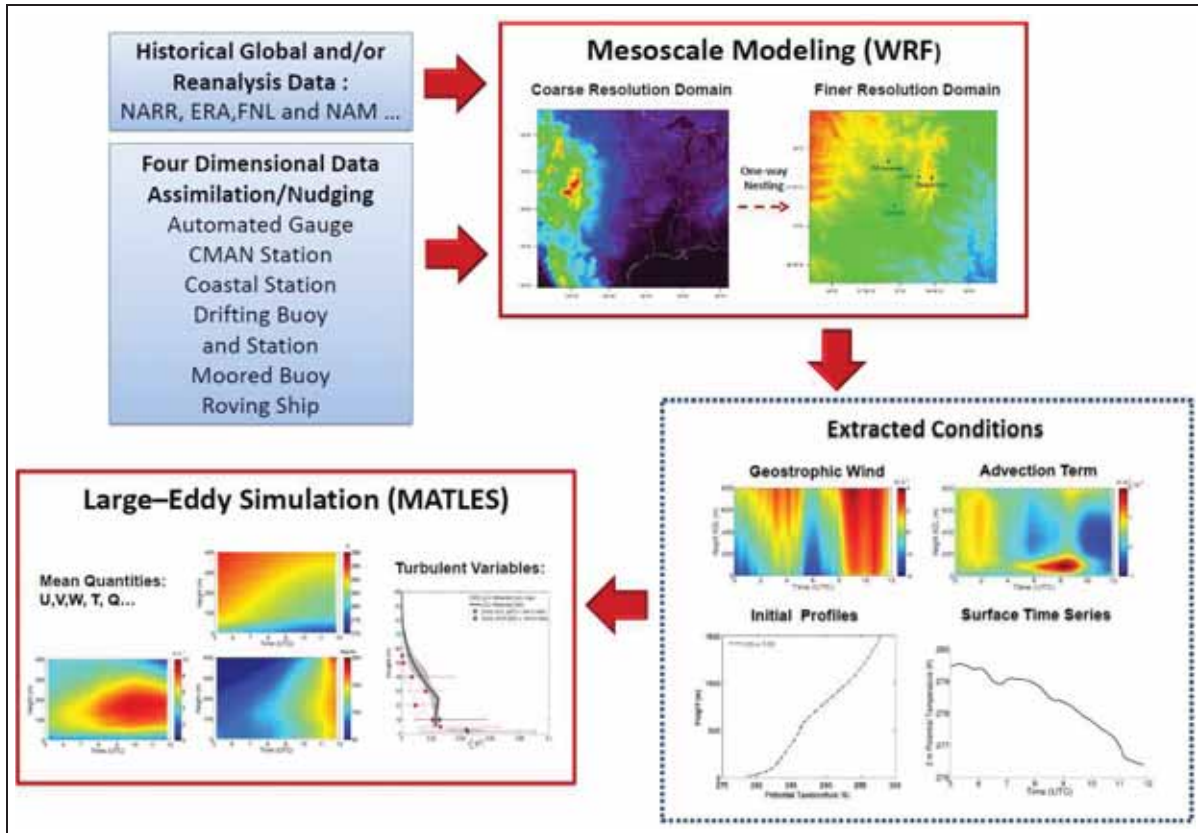


FIG. 1: Procedure for generating realistic turbulence utilizing a coupled mesoscale and large-eddy modeling framework.

154 Rizza et al.⁷⁴ did not incorporate radiation physics in their LES model. Other technical
 155 differences are in numerical configurations, LES subgrid-scale (SGS) modeling, geostrophic
 156 wind estimation strategy, etc. Also, our selected nighttime case study is more scientifically
 157 challenging than the daytime case simulated by Rizza et al.⁷⁴.

158 IV. DESCRIPTION OF CASE STUDY

159 In this paper, we simulated a nocturnal stable boundary layer observed during the period,
 160 October 23-24, 1999 as part of the Cooperative Atmosphere-Surface Exchange Study - 1999
 161 (CASES-99) field campaign⁷¹. This particular case is quite interesting due to the existence
 162 of intermittent turbulence, as well as due to the presence of a moderately strong low-level jet.
 163 On this night, the mid-west United States (encompassing the CASES-99 site) was dominated

164 by a high-pressure system (see Fig. 2). At the CASES-99 site, the sky was virtually cloud-
165 free, setting the stage for a moderately/strongly stratified boundary layer. Other synoptic
166 conditions for this case were discussed by Shin and Hong⁷⁷ and will not be repeated here for
167 brevity.

168 The CASES-99 field site was located near Leon, Kansas (37.65° N, 96.74° W). The rel-
169 atively flat terrain and uniform roughness ($z_o = 0.03$ m) of this site make it attractive for
170 boundary layer studies. Please refer to Fig. 3 for a depiction of the topographical features
171 around this field site.

172 The selected case study was earlier simulated by several researchers utilizing single-
173 column, mesoscale, and large-eddy models: Steeneveld et al.⁸¹, Steeneveld et al.⁸², Kumar
174 et al.⁴⁶, Shin and Hong⁷⁷, and Svensson et al.⁸⁹. Based on these past studies, we were able
175 to better understand the challenges associated with the selected case study. Furthermore,
176 some of these studies helped us to decide on certain mesoscale model configurations (see
177 Section VI for details).

178 V. DESCRIPTION OF OBSERVATIONAL DATASETS

179 In this work, a diverse suite of observational datasets was utilized for model validation.
180 These datasets were collected by a doppler lidar, a small-aperture scintillometer, several
181 sodars, sonic anemometers, and a sounding system. Used in a complementary fashion, these
182 datasets increased the reliability of the nocturnal turbulence characterization. The basic
183 characteristics of these datasets are provided in Table I. For detailed descriptions (including
184 working principles of the instruments, data acquisition, calibration, accuracy, etc.) please
185 refer to the references listed in Table I.

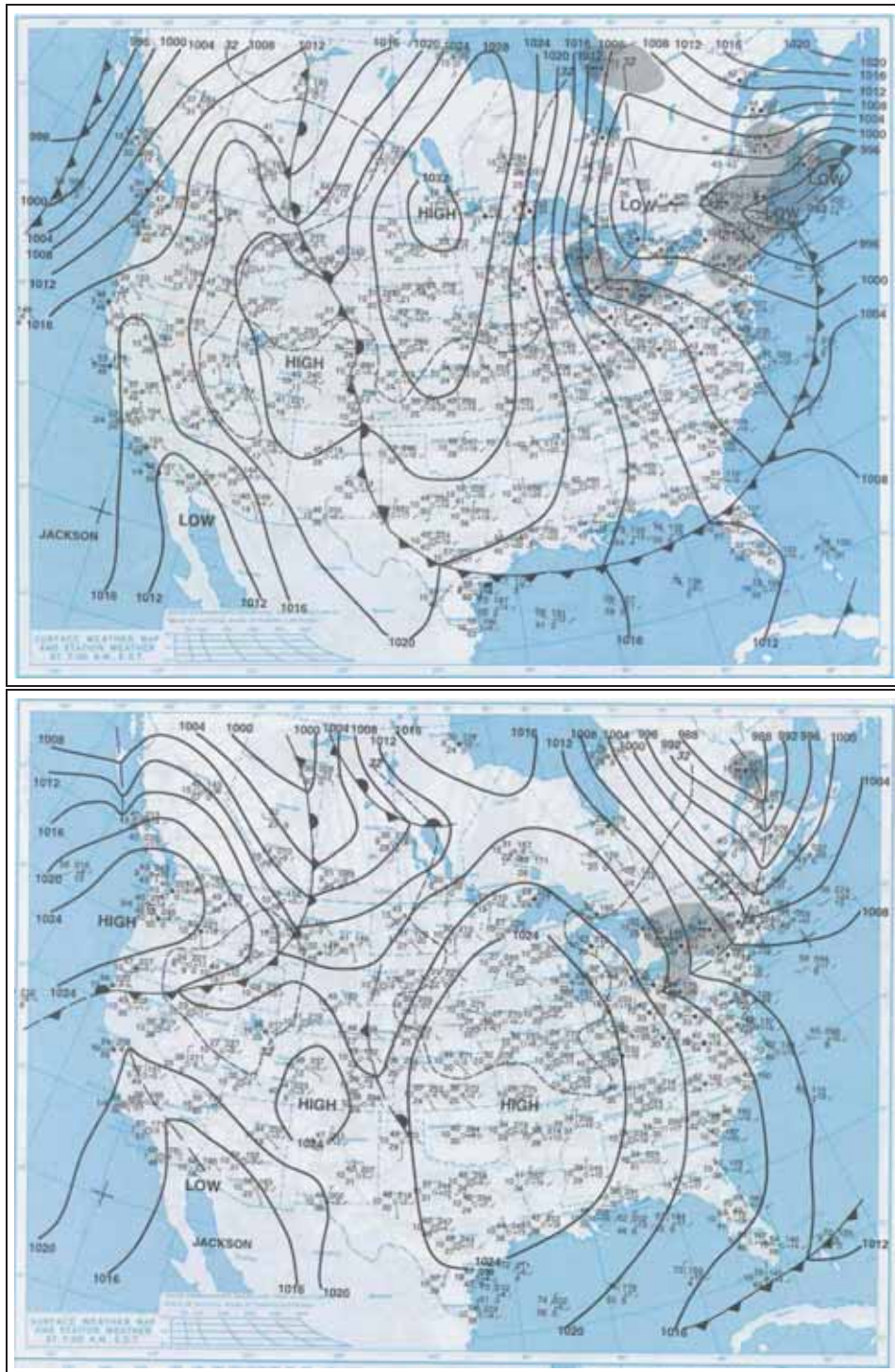


FIG. 2: Surface analysis at 12 UTC on October 23, 1999 (top panel) and October 24, 1999 (bottom panel). The Midwest United States was dominated by a synoptic-scale surface high-pressure system during this time period. Source: <http://www.hpc.ncep.noaa.gov/dailywxmap/>

TABLE I: Basic characteristics of the observational datasets

Instrument	Variables*	Frequency	Vertical Coverage	References
Lidar	M, σ_u^2	1 Hz	$\approx 0 - 400$ m AGL	6,69,71
Scintillometer	$u_*, \langle w'\theta' \rangle$	every 6 s	≈ 2.5 m AGL	31,32
Sodar	M, X	every min	$30 \approx 0 - 200$ m AGL	18,28,71
Sonic-EOL	$M, X, \sigma_u^2, \sigma_v^2, \sigma_w^2, \sigma_\theta^2,$ $u_*, \langle w'\theta' \rangle$	20 Hz	$\approx 0 - 60$ m AGL	71,88
Sonic-WUR	$M, X, \sigma_u^2, \sigma_v^2, \sigma_w^2, \sigma_\theta^2,$ $u_*, \langle w'\theta' \rangle$	20 Hz	≈ 3 m, 10 m AGL	31,71
Sounding	M, X, Θ, Q	a few times per day	several km AGL	6,71

¹⁸⁶ *Relevant variables are defined as follows:

M : wind speed (m s^{-1})

X : wind direction (degrees)

Θ : potential temperature (K)

Q : specific humidity (kg kg^{-1})

u_* : friction velocity (m s^{-1})

¹⁸⁷ $\langle w'\theta' \rangle$: sensible heat flux (K m s^{-1})

σ_u^2 : variance of longitudinal velocity component ($\text{m}^2 \text{s}^{-2}$)

σ_v^2 : variance of lateral velocity component ($\text{m}^2 \text{s}^{-2}$)

σ_w^2 : variance of vertical velocity component ($\text{m}^2 \text{s}^{-2}$)

σ_θ^2 : variance of potential temperature (K^2)

¹⁸⁸ The acronyms EOL and WUR in Table I stand for Earth Observing Laboratory of the Na-
¹⁸⁹ tional Center for Atmospheric Research (NCAR) and Wageningen University and Research
¹⁹⁰ Centre, respectively.

191 VI. MESOSCALE MODELING

192 In this study, Version 3.3.2 of the Weather Research and Forecasting (WRF) model was
193 utilized for mesoscale simulations. This state-of-the-art, non-hydrostatic model includes
194 numerous atmospheric physics parameterizations and advanced data assimilation modules⁷⁹.
195 Over the past few years, the WRF model has been developed by the collaborative efforts
196 of multiple organizations such as the National Center for Atmospheric Research (NCAR),
197 the National Oceanic and Atmospheric Administration (NOAA), universities, and others.
198 Several recent studies (e.g.,^{24,27,42,64,85}) have demonstrated the strengths of the WRF model
199 in simulating various mesoscale atmospheric phenomena (including LLJs).

200 In Section IV, we mentioned that Steeneveld et al.⁸² performed an intercomparison study
201 of several MMMs for the selected case study. They reported:

202 “All schemes underestimate the diurnal temperature cycle amplitude and the
203 near-surface stability at night. None of the parameterizations was able to repre-
204 sent the surface radiation and turbulent fluxes, the wind speed and temperature
205 profiles, and the boundary layer height correctly during the full diurnal cycle.
206 Schemes with local mixing provide a more realistic representation of the night-
207 time boundary layer, especially for weak winds, and when the asymptotic length
208 scale is based on the flow properties. Moreover, the nighttime low-level jet is
209 hard to reproduce, and we find a clear dependence on the chosen model domain
210 size.”⁸²

211 These findings provided valuable guidance in our selection of the WRF domain size and
212 the planetary boundary layer (PBL) scheme. The selection of other numerical settings and
213 physical parameterizations was largely based on our past experience^{64,85,86}.

214 We used a large outer domain (resolution: 27 km) of dimensions 2700 km \times 2700 km
215 centered on Leon, KS (see the top left panel of Fig. 3). This domain size was sufficient for
216 reliable LLJ simulations. Three one-way nested domains with resolutions of 9 km, 3 km,
217 and 1 km were set up inside this outer domain. Also, 51 non-uniformly spaced vertical grid
218 levels with approximately 7 levels below 200 m were used (top right panel of Fig. 3).

219 Shin and Hong⁷⁷ conducted an extensive PBL scheme sensitivity experiment for the se-
220 lected case study. They reported tremendous variability among simulations utilizing different
221 PBL schemes; more importantly, they were unable to identify a clear ‘winner’ among the

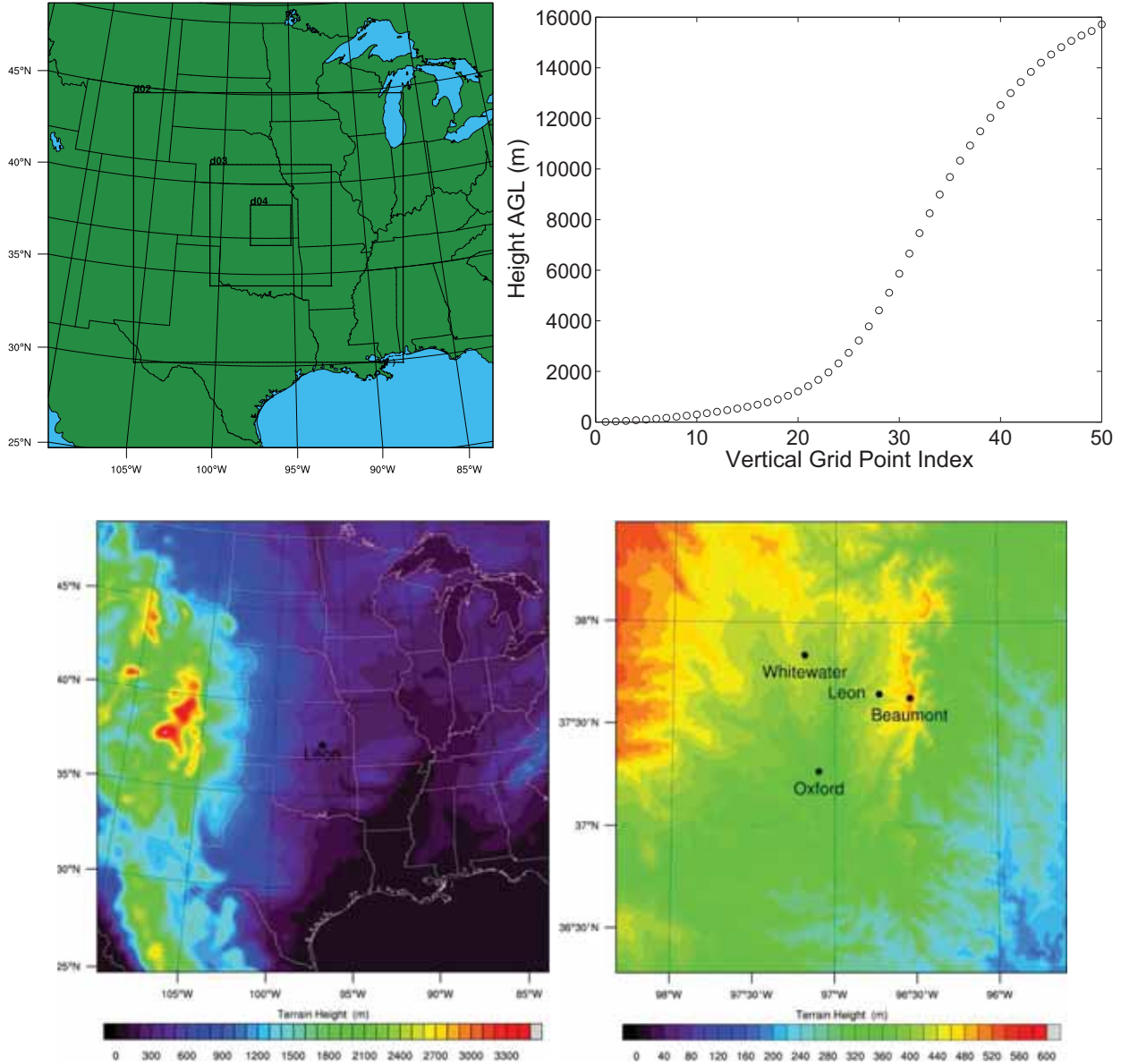


FIG. 3: The WRF model runs utilize four nested domains (top left panel) of grid resolutions 27/9/3/1 km. The locations of the vertical grid points are shown in the top right panel. The elevation maps of the coarsest and the finest domains are shown in the bottom left and bottom right panels, respectively. The locations of various observational sites are marked on these panels.

222 various PBL schemes. For this reason, following Occam’s razor principle, we chose one of
 223 the simplest PBL schemes available with the WRF model—the Yonsei University (YSU)
 224 scheme^{35,36}. This first-order scheme utilizes the K-profile approach^{19,65,84,91} and is numer-

225 ically very stable¹⁶. Recently, H. Richardson and S. Basu discovered a numerical bug in
226 the YSU scheme. This bug has been corrected in Version 3.4.1 of the WRF model. In the
227 present study, we used an older version of the WRF model in conjunction with the bug fix.

228 The following other physical parameterizations were selected in this study: (i) micro-
229 physics: WRF Single-Moment 5-class scheme³⁷; (ii) shortwave and longwave radiation:
230 Rapid Radiative Transfer Model for Global Climate Models (RRTMG) scheme^{38,58}; (iii)
231 cumulus: Kain-Fritsch scheme^{40,41}; and (iv) land surface: Noah scheme²³. The cumulus
232 scheme was switched on only for the domains with 27 km and 9 km resolutions. For the
233 finer resolution domains, the cloud processes were simulated explicitly. These parameteri-
234 zation schemes are discussed in great detail by Stensrud⁸⁴.

235 We performed two mesoscale simulations using the aforementioned numerical and phys-
236 ical settings. In one of the simulations (called WRF-SN), we invoked the so-called four-
237 dimensional data assimilation (FDDA) technique^{50,51,80} to assimilate the public-domain
238 NCEP ADP Global Surface Observational Weather Data¹. We wish to note that the diverse
239 observational datasets described in the previous section were not assimilated; they were
240 solely used for model validation. The FDDA configuration details are summarized below:

- 241 • the nudging coefficient for both wind and temperature was set equal to $6 \times 10^{-4} \text{ s}^{-1}$;
242 this is the default value in the WRF model;
- 243 • the horizontal radii of the nudging influence for all the variables were chosen as ten
244 times the grid size (e.g., the horizontal influence of the finest domain is $10 \times 1 \text{ km} =$
245 10 km);
- 246 • the vertical radii of the nudging influence were defined on the η levels and were set
247 equal to 0.002;
- 248 • the half-period time width was defined as 10 min (i.e., the WRF model searches for
249 observed data 10 min before and 10 min after the current integration time).

250 The other mesoscale simulation (called WRF-NN) did not include any data assimilation.

251 The initial and boundary conditions from the North American Regional Reanalysis
252 (NARR; spatial resolution: 32 km; temporal resolution: 3 h) dataset were used for both

¹ <http://rda.ucar.edu/datasets/ds464.0/>

253 the WRF simulations. The simulations started at 12 UTC on 23 October and continued for
 254 almost 24 hours; the last 7 h of the simulations (from local midnight to sunrise) are reported
 255 on in this paper. The WRF model output was stored every 10 min for a comprehensive
 256 analysis and for synthesis of the input data for the LES runs.

257 Most of the modeling results are presented in Section VIII. However, in the present
 258 section, we discuss two issues related to the mesoscale modeling of SBLs and LLJs: (i)
 259 spatio-temporal error and (ii) spatial variability.

260 In Fig. 4, the WRF model-simulated wind speeds are compared with lidar-based ob-
 261 servations at Leon. The following discrepancies between observed and modeled data are
 262 evident:

- 263 • the WRF model simulated a weaker and slightly higher LLJ;
- 264 • the timings of the observed and modeled LLJ peaks are quite different.

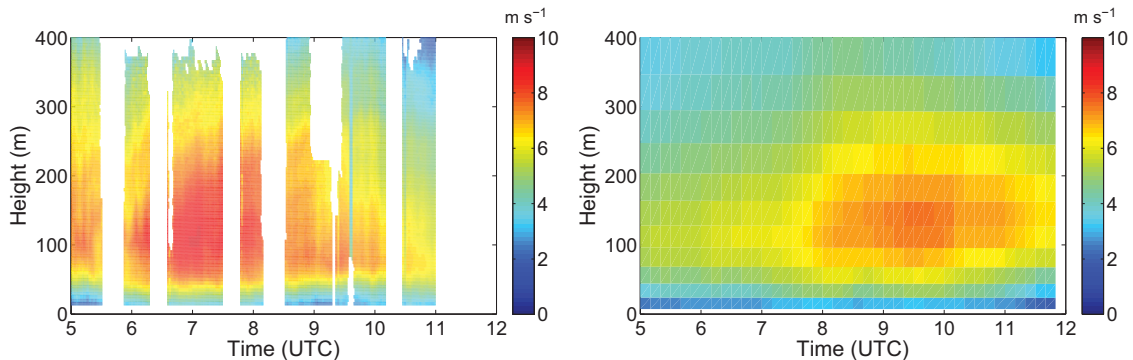


FIG. 4: Time-height plots of lidar-based (left panel) and WRF model-simulated (right panel) wind speeds.

265 It is well-known from the literature (e.g.,^{25,86}) that the MMMs usually create weaker and
 266 higher LLJs due to enhanced diffusion. The simulations reported by Steeneveld et al.⁸² and
 267 Shin and Hong⁷⁷ also support this fact. Therefore, the first discrepancy is in line with the
 268 literature.

269 The second disagreement between data and model is, however, unexpected. According
 270 to Blackadar’s inertial oscillation hypothesis^{87,93}, the peak of the LLJ at Leon should occur
 271 ≈ 9.8 h after sunset². On October 24, 1999, sunset at Leon occurred at 23:40 UTC; thus, the

² The latitude at Leon is 37.65° N. The corresponding Coriolis parameter, f , is $8.9 \times 10^{-5} \text{ s}^{-1}$. The LLJ peak should occur at $\pi/f = 9.8$ h after frictional decoupling at sunset.

272 LLJ peak maximum was expected to occur around 9:30 UTC. The WRF model simulated
 273 the LLJ peak maximum exactly at this time. Interestingly, the observed LLJ peak occurred
 274 3 h earlier. It is likely that some other dynamical mechanisms were responsible for this
 275 behavior, which were not captured by the WRF model.

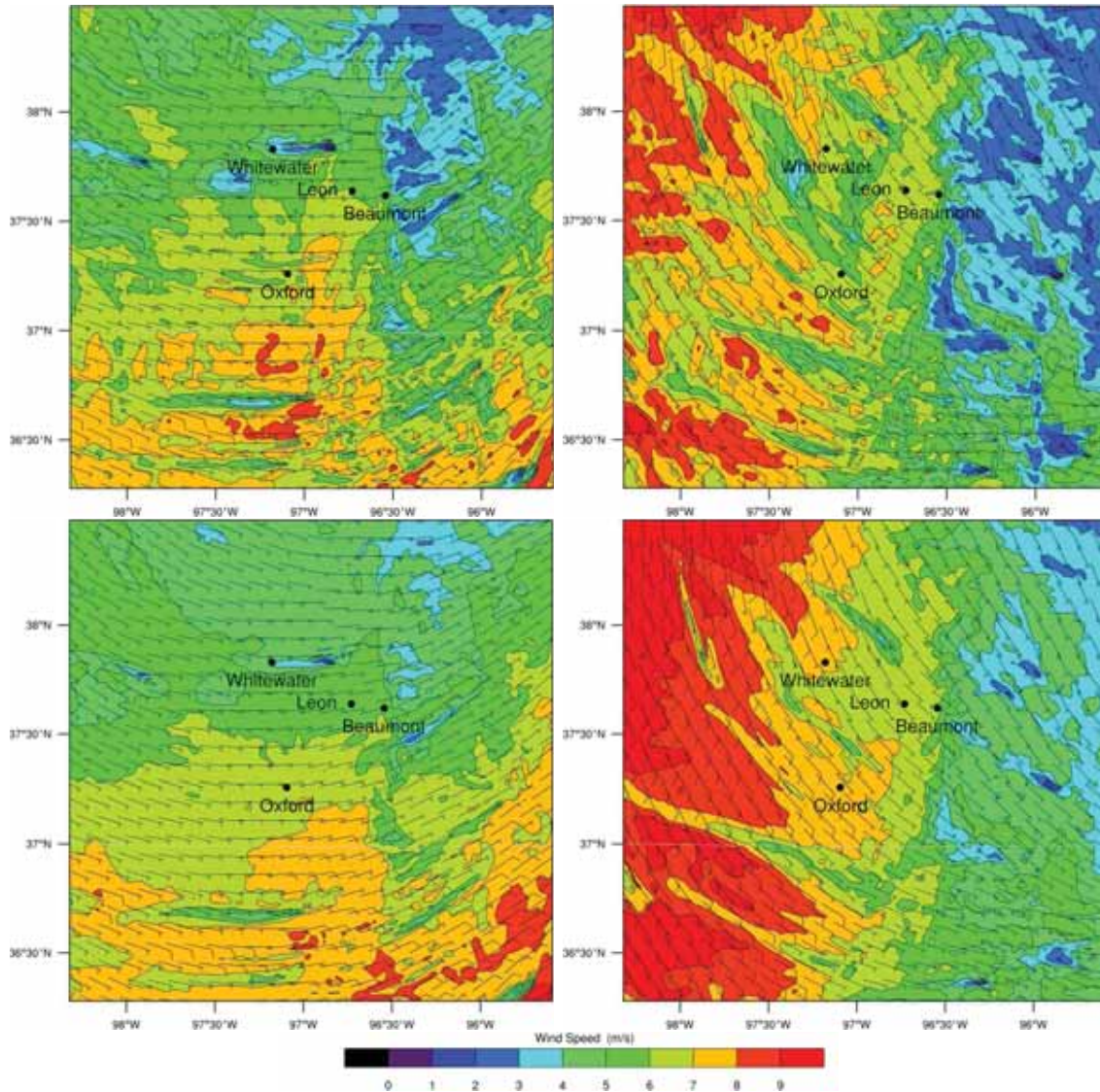


FIG. 5: The WRF model-based simulated wind speeds and wind barbs at 90 m (top panels) and 150 m (bottom panels) above ground level. The left and right panels represent 7 UTC and 11 UTC, respectively, on October 24, 1999. The locations of various observational sites are marked on these panels.

276 The WRF model-based simulated wind speeds and wind barbs at 90 m (top panels) and

277 150 m (bottom panels) above ground level (AGL) are shown in Fig. 5. The left and right
 278 panels represent 7 UTC and 11 UTC, respectively, on October 24, 1999. From this figure, it
 279 is clear that the nocturnal wind fields are extremely variable. Similar conclusions can also
 280 be drawn from Fig. 6 which shows sodar-based wind field evolutions from four neighboring
 281 locations (on relatively flat terrain): Beaumont, Leon, Oxford, and Whitewater.

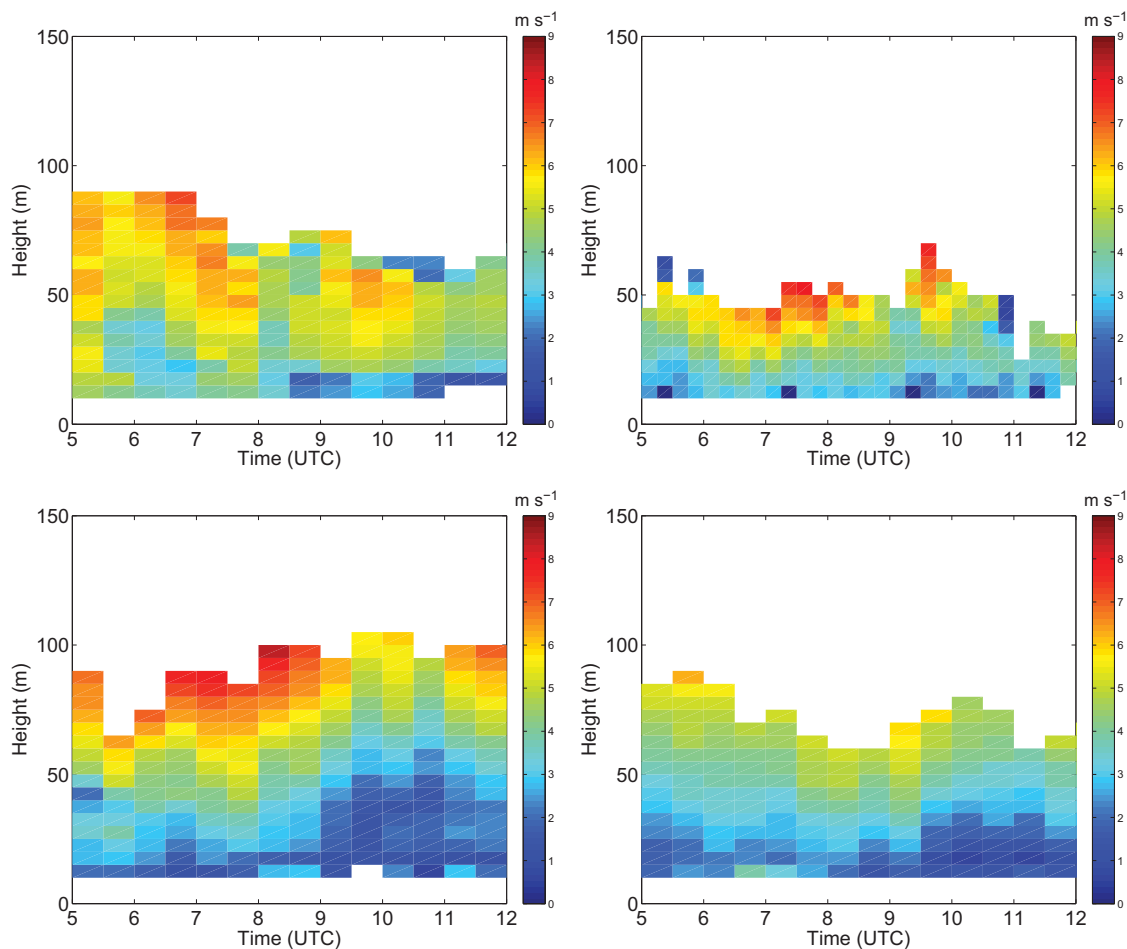


FIG. 6: Time-height plots of sodar-measured wind speeds at Beaumont (top left panel),
 Leon (top right panel), Oxford (bottom left panel), and Whitewater (bottom right panel).

282 The spatio-temporal variabilities of wind fields shown in Figs. 4-6 have strong implications
 283 from a model validation perspective. We speculate that similar (or perhaps stronger) spatio-
 284 temporal variabilities exist in the nocturnal turbulence fields. At the same time, high-quality
 285 turbulence observations are only available from a single location: Leon. This lack of spatio-
 286 temporal observations causes reliable model validation to be a challenging if not impossible

287 task. Thus, the model validation results presented in Section VIII should be studied with
288 some degree of caution.

289 VII. LARGE-EDDY SIMULATION

290 In this study, an in-house model, MATLES, is utilized for the large-eddy simulations. It
291 utilizes the locally-averaged scale-dependent dynamic (LASDD) subgrid-scale (SGS) model.
292 The most recent version of this model includes Version 2.1.7 of the Column Radiation scheme
293 (CRM;⁴⁴). Other technical details of the MATLES model have been described in various
294 publications (e.g.,^{12,73}) and will not be repeated here for brevity.

295 The LES runs were initialized with the WRF model-generated mean profiles for Leon at 5
296 UTC (local midnight), October 24, 1999 (not shown). This particular initialization time was
297 chosen to reduce the impact of the residual layer turbulence on the SBL simulations. A sim-
298 ilar strategy was used for the GEWEX Atmospheric Boundary Layer Study (GABLS) third
299 LES intercomparison project¹³. In idealized simulations, small-scale random perturbations
300 (noise) are typically added to the initial profiles. In this work, more realistic noise profiles
301 were generated utilizing Nieuwstadt’s local scaling approach^{10,62}. Specifically, for horizontal
302 velocity fields, we used Gaussian noise with zero mean and variance equal to $4u_*^2(1 - z/h)^{3/2}$
303 for $z < h$. However, for the potential temperature field, we used Gaussian noise with zero
304 mean and variance equals to $9\theta_*^2$ for $z < h$. Based on the WRF model-generated profiles of
305 wind speed and potential temperature, the height, h , of the SBL at 5 UTC was estimated
306 to be equal to 100 m. The values of surface friction velocity (u_*) and surface temperature
307 scale (θ_*) were also extracted from the WRF model-based simulations.

All the simulations were run for ≈ 7 h until 11:50 UTC (sunrise time was 12:44 UTC).
The lower boundary conditions were based on the Monin-Obukhov similarity theory with
a surface roughness length, $z_o = 0.03$ m⁸⁹. The WRF model-simulated time series for 2 m
potential temperature and 2 m specific humidity were used for lower boundary conditions (see
Fig. 7). The overall cooling rate at 2 m was ≈ 0.25 K h⁻¹. The specific humidity remained
almost constant over the entire simulation period. During the simulations, the surface
sensible heat flux ($\langle w'\theta' \rangle$) was estimated using both the prescribed potential temperature

(Θ_2) and the mean potential temperature ($\Theta(z_1)$) at the model's lowest level (z_1) as follows:

$$\langle w'\theta' \rangle = \frac{\kappa u_* [\Theta_2 - \Theta(z_1)]}{\log\left(\frac{z_1}{2}\right) - \psi_H\left(\frac{z_1}{L}\right) + \psi_H\left(\frac{2}{L}\right)} \quad (1)$$

308 where L is the Obukhov length; κ is the von Kármán constant ($= 0.4$); and $\psi_H\left(\frac{z_1}{L}\right) = -5z/L$
 309 for stably stratified conditions⁴. A similar approach was followed for the surface latent heat
 310 flux estimation. Please refer to Basu et al.¹² for a description of the surface shear stress
 311 estimation procedure.

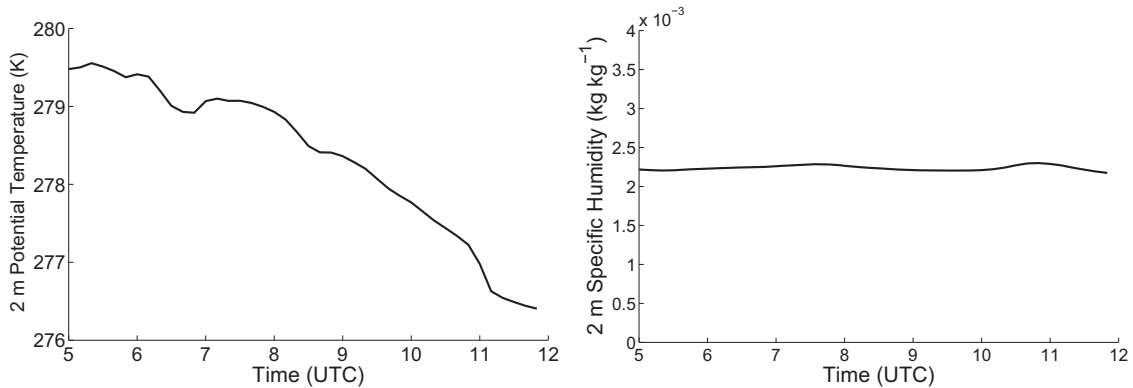


FIG. 7: The WRF model-simulated time series of 2 m potential temperature (left panel) and 2 m specific humidity (right panel). These data were used as lower boundary conditions for the LES runs.

312 In the past, numerous SBL modeling studies that have been undertaken used the sensible
 313 heat flux as a lower boundary condition^{21,39,75}. In Basu et al.¹¹, the fundamental short-
 314 comings of such sensible heat flux-based lower boundary conditions were discussed. Based
 315 on analytical and numerical results, it was shown that, if the surface sensible heat flux
 316 is prescribed as a boundary condition, only the near-neutral to weakly stable regimes are
 317 captured. In order to represent moderate to very stable regimes in simulations, surface
 318 temperature prescription or prediction is required. Holtslag et al.³⁴ provide further insights
 319 into this topic. For these reasons, we used near-surface potential temperature as a lower
 320 boundary condition.

321 In contrast to the aerodynamic roughness length (z_o), the thermal roughness length (z_{oT})
 322 is not as well understood and there is no consensus in the literature regarding the $z_o - z_{oT}$
 323 relationship. Thus, we used 2 m potential temperature instead of the surface temperature;
 324 based on Eq. 1, it is clear that z_{oT} was not needed in our approach.

325 The upper boundary consisted of a zero stress condition, whereas the lateral boundary
 326 conditions assumed periodicity. A Rayleigh damping layer at 550 m was used. Potential
 327 temperature and specific humidity gradients were guided by the WRF output and prescribed
 328 at the upper boundary as follows: $d\Theta/dz = 0.0142 \text{ K m}^{-1}$, $dQ/dz = 2.468 \times 10^{-6} \text{ Kg Kg}^{-1}$
 329 m^{-1} .

330 Time-height-dependent geostrophic wind components (U_g, V_g) were estimated from the
 331 WRF model-generated pressure fields (Fig. 8). In order to avoid local-scale (smaller than the
 332 meso- β scale of 20 km) perturbations, the estimated geostrophic wind fields were spatially
 333 filtered (over horizontal planes) using a moving average filter of $20 \text{ km} \times 20 \text{ km}$ stencil
 334 size. The presence of strong baroclinicity (likely due to the sloping terrain of the U.S. Great
 335 Plains) is evident in Fig. 8 and should always be accounted for in realistic simulations.

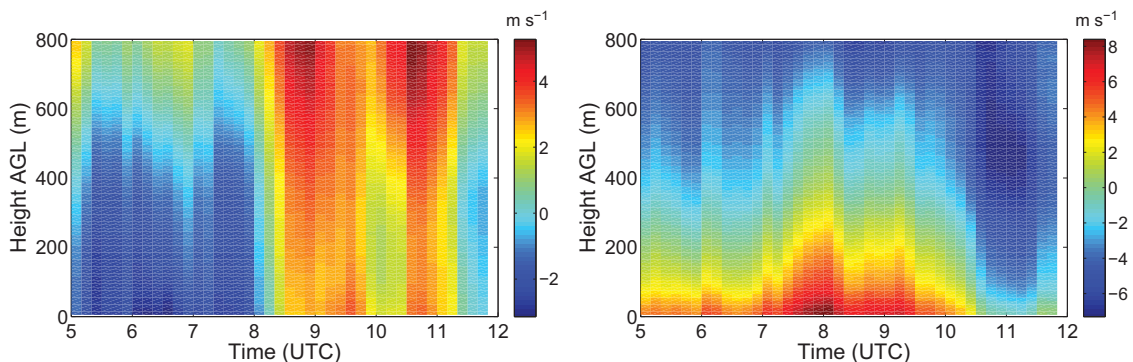


FIG. 8: Time-height plots of the WRF model-simulated zonal (east-west; left panel) and meridional (north-south; right panel) geostrophic wind components.

336 Similar to the geostrophic wind fields, the time-height-dependent mesoscale advection
 337 terms (for momentum, heat, and moisture) were also obtained from the WRF-generated
 338 fields (Fig. 9). These fields were also spatially filtered with a stencil size of $20 \text{ km} \times 20 \text{ km}$.
 339 We would like to point out that we neglected the vertical component of advection in our
 340 calculations. In other words, for a generic variable, Φ , the advection term is defined as:

$$ADV_{\Phi} = - \left(U \frac{\partial \Phi}{\partial x} + V \frac{\partial \Phi}{\partial y} \right) \quad (2)$$

341 Mesoscale advection terms are usually neglected in LES studies (one of the exceptions
 342 being the GABLS third LES intercomparison case;¹³). However, these terms could be sig-

343 nificant for realistic simulations. For example, from Fig. 9, it is clear that a large amount
 344 of low-level temperature advection (up to $\approx 0.7 \text{ K h}^{-1}$) occurred during 5-12 UTC. This
 345 additional heat source reduced the bulk stability and generated a deeper SBL. The following
 346 section discusses this topic in greater detail.

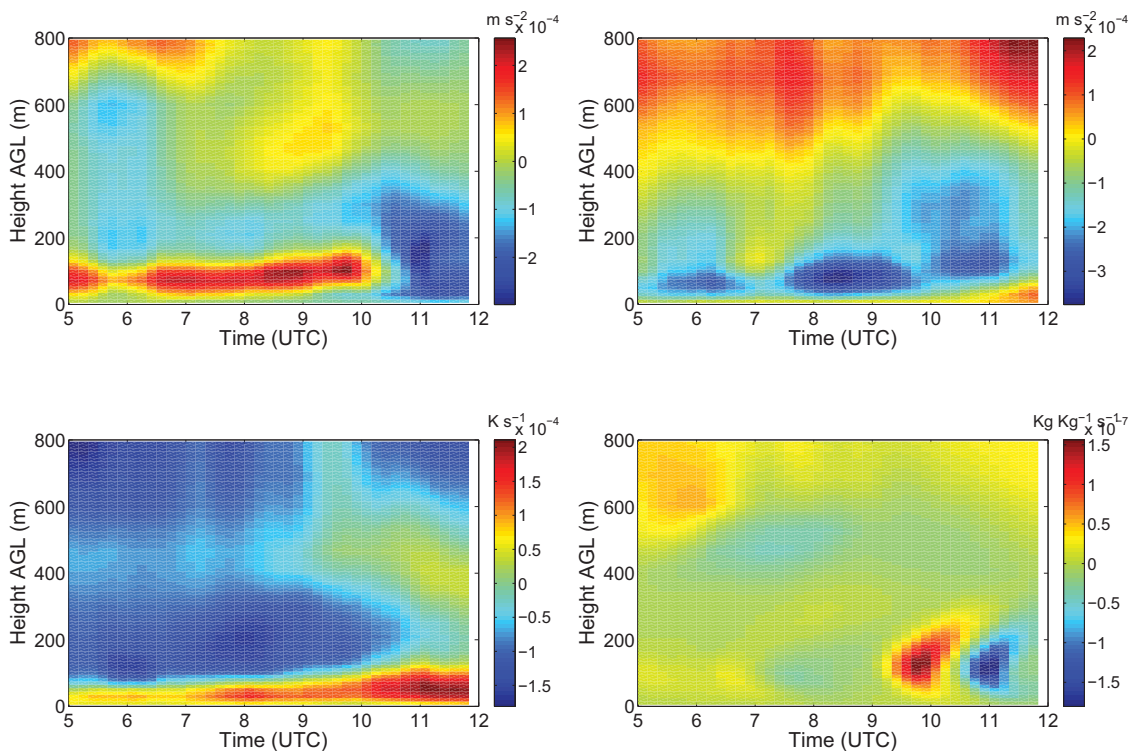


FIG. 9: Time-height plots of the WRF model-simulated mesoscale advection terms: zonal wind component (top left panel), meridional wind component (top right panel), potential temperature (bottom left panel), and specific humidity (bottom right panel).

347 Recently, Mirocha and Kosović⁵⁷, studied the influence of subsidence on SBL simulations.
 348 The impacts of changing the subsidence from zero to 0.002 m s^{-1} was substantial in terms
 349 of the depth, mixing, and cooling rate of the SBL. Svensson et al.⁸⁹ also considered a
 350 constant subsidence of 0.005 m s^{-1} in their simulation of the GABLS second single-column
 351 model intercomparison study. They estimated subsidence from a mesoscale output. In the
 352 present work, we also attempted to estimate subsidence from the WRF model output (see
 353 Fig. 10). Subsidence was found to be spatio-temporally highly intermittent. Moreover, we
 354 were unable to isolate the topographical effect from the synoptic-scale atmospheric effect.

355 Given the uncertainty in its estimation, we decided not to include subsidence in the LES
 356 runs. In retrospect, we believe that this exclusion resulted in slightly deeper SBLs in the
 357 LES runs in comparison to the WRF model results.

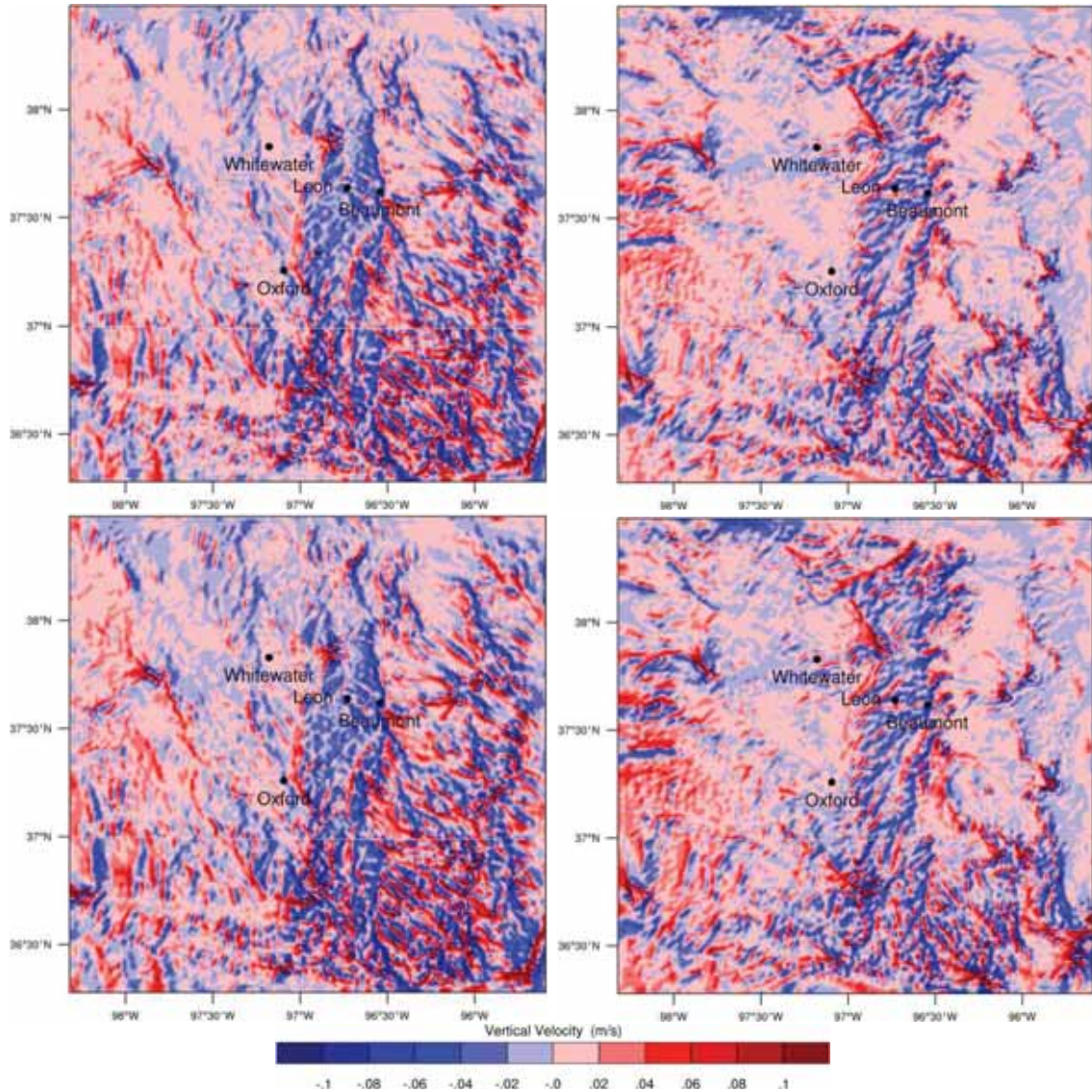


FIG. 10: The WRF model-based simulated vertical velocity at 90 m (top panels) and 150 m (bottom panels) above ground level. The left and right panels represent 7 UTC and 11 UTC, respectively, on October 24, 1999. The locations of various observational sites are marked on these panels.

358 The selected domain size for all the LES runs was $800 \text{ m} \times 800 \text{ m} \times 790 \text{ m}$, divided
 359 into $80 \times 80 \times 80$ grid points (i.e., the grid resolution was $10 \text{ m} \times 10 \text{ m} \times 10 \text{ m}$). The

360 land surface was assumed to be flat which is a realistic assumption for the selected location
 361 near Leon. The time step was equal to 0.125 s, while each run was ≈ 7 h (i.e., 196,800
 362 time-steps) in duration. In order to assess the influence of the grid resolution on the results,
 363 we performed two runs with $64 \times 64 \times 64$ grid points ($\Delta x = 12.5$ m \times $\Delta y = 12.5$ m \times
 364 $\Delta z = 12.5$ m; $\Delta t = 0.2$ s) and $40 \times 40 \times 40$ grid points ($\Delta x = 20$ m \times $\Delta y = 20$ m \times
 365 $\Delta z = 20.3$ m; $\Delta t = 0.4$ s), respectively. In addition, two more LES runs were performed to
 366 assess the impacts of radiation and mesoscale advection on the simulated results. Table II
 367 summarizes the configurations of all the LES runs. Planar-averaged profiles were output
 368 every 10 min from these simulations. For spectral analysis, time series data from selected
 369 grid points were output every time step.

TABLE II: List of LES runs and associated configurations

Run	Spatial Resolution	Radiation Scheme	Mesoscale Advection
L80-A-R-SN	10.0 m \times 10.0 m \times 10.0 m	Yes	Yes
L80-A-SN	10.0 m \times 10.0 m \times 10.0 m	No	Yes
L80-SN	10.0 m \times 10.0 m \times 10.0 m	No	No
L64-A-R-SN	12.5 m \times 12.5 m \times 12.5 m	Yes	Yes
L40-A-R-SN	20.0 m \times 20.0 m \times 20.3 m	Yes	Yes

370 VIII. RESULTS

371 In this section, simulated mean profiles from the WRF and MATLES models are first com-
 372 pared. The similarity of the results would indicate that the forcing terms (i.e., geostrophic
 373 winds and mesoscale advection terms) were appropriately extracted from the WRF output.
 374 It would also indicate that the physical parameterizations (e.g., microphysics), which are
 375 present in the WRF model, but absent in the MATLES model, were not important for this
 376 clear-sky case.

377 Next, the modeled results are validated against a diverse set of observations. Given the
 378 spatio-temporal variabilities of the observations and the simulated results (see Section VI),
 379 as well as the apparent inconsistencies among different observational platforms (discussed
 380 below), we argue that it is not necessary to place undue emphasis on the quantitative

381 differences. On the other hand, qualitative trends and some similarity statistics (e.g., in
382 temporal spectra) should provide valuable insights.

383 **A. First-Order Statistics**

384 The time-height plots of the simulated wind speed, wind direction, potential temperature,
385 and specific humidity are shown in Fig. 11. For the WRF model results, the vertical profiles
386 represent instantaneous values from the grid point closest to Leon. In the case of the
387 MATLES results, these profiles represent planar-averaged values from the entire domain.

388 The timing of the LLJ event as well as the temporal evolution of the wind direction
389 profiles are similar in both the mesoscale and the LES results. This qualitative similarity
390 suggests that the dynamical forcings are similar in both the simulations. However, the LLJ
391 is stronger and slightly higher in the case of the LES results. It is widely known that the
392 strength of the LLJs is strongly dependent on the diffusion of the associated SBL. Given
393 that the strength of the LES-generated jet is more similar to the observed one (see the left
394 panel of Fig. 4) than is the case for the WRF-generated one, we conclude that the LES has
395 captured the nighttime mixing with greater fidelity than the YSU PBL scheme of the WRF
396 model. Since the LES run did not include subsidence, the simulated LLJ height is slightly
397 higher. This feature is also visible in the time-height plot of the potential temperature—the
398 LES generated a slightly deeper SBL. The evolution of specific humidity is very similar in
399 the mesoscale and LES results. Due to accurate prescription of the mesoscale advection, the
400 LES run has even captured a short burst of moisture enhancement during 10-11 UTC. This
401 enhancement could be due to a small-scale frontal passage.

402 As the observed sounding data were available at 7 and 11 UTC, we chose those specific
403 times for comparison of the observed and simulated vertical profiles (Figs. 12 and 13). In
404 addition to the sounding data, we overlaid data collected by a doppler lidar (wind speed
405 only) and a meteorological tower (wind speed and wind direction). It is quite interesting to
406 see that the lidar-based wind speed observations are quite different in magnitude from the
407 sounding observations. Banta et al.⁶ mentioned some technical issues related to the sounding
408 launches during the CASES-99 field campaign, which might explain the differences. Since
409 other publications (e.g.,^{77,82}) compared simulated results against these soundings, we decided
410 not to exclude them in this paper.

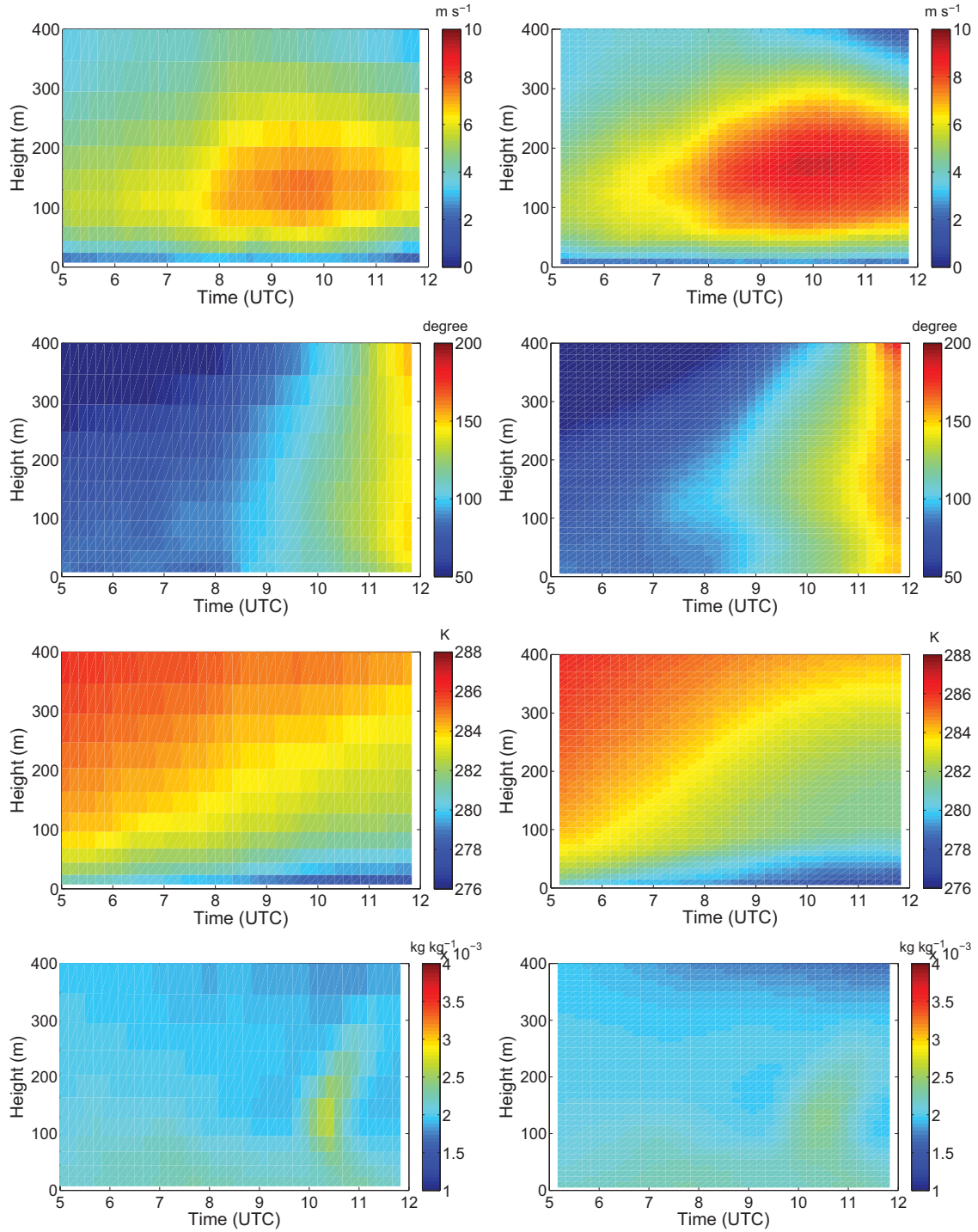


FIG. 11: Time-height plots of simulated wind speed (top panels), wind direction (second panels), potential temperature (third panels), and specific humidity (bottom panels). The left and right panels represent results from the WRF model and the MATLES model, respectively.

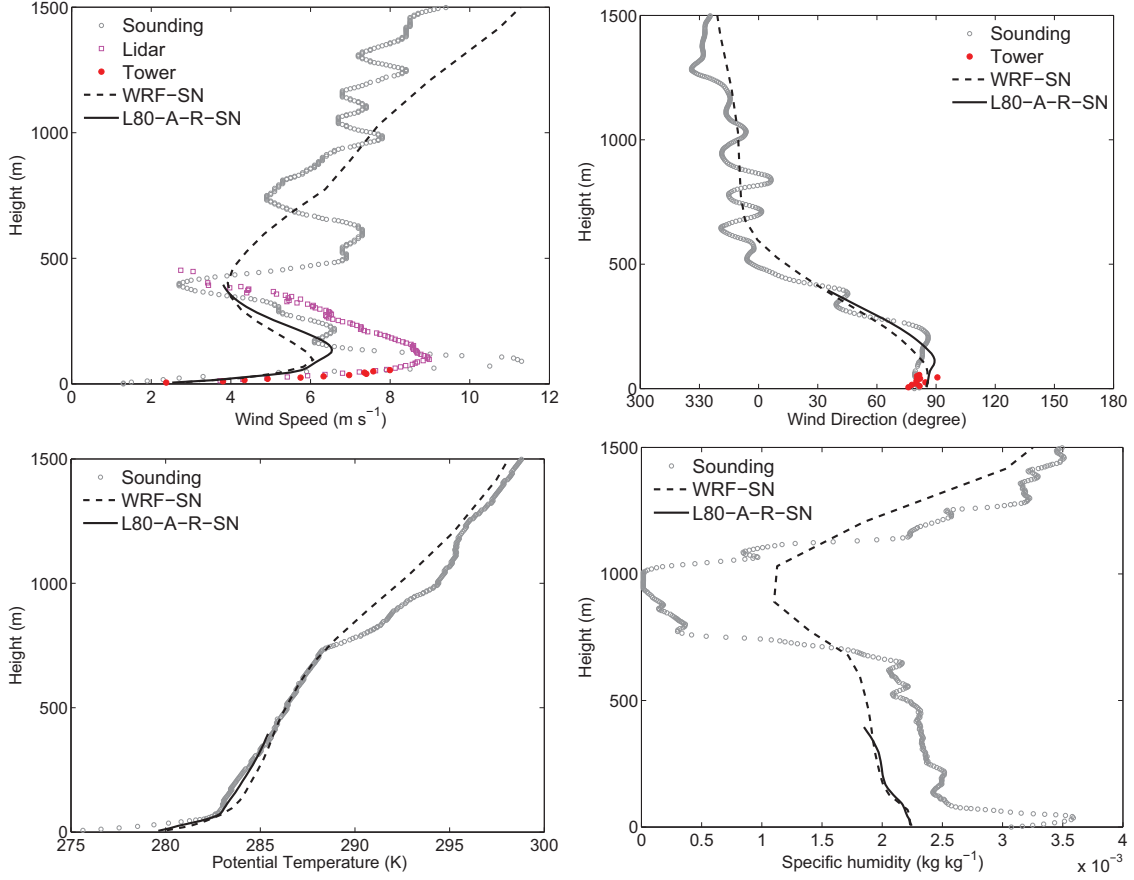


FIG. 12: Plots of the wind speed (top left panel), wind direction (top right panel), potential temperature (bottom left panel), and specific humidity (bottom right panel) profiles corresponding to 7 UTC.

411 Considering, first, the profiles from 7 UTC presented in Fig. 12, we note that the heights
 412 of the lidar-based and the WRF-based LLJs are quite similar. As explained before, the
 413 LES-based LLJ is slightly higher due to the lack of subsidence. The observed and simulated
 414 wind shears agree very well in the lower part of the SBL. Differences in the modeled and
 415 observed LLJ are largely due to the temporal shift in their evolution.

416 The WRF and LES models captured the wind direction and potential temperature profiles
 417 remarkably well. The wind direction within the SBL ($h \approx 100$ m) was from the east; however,
 418 at higher elevations, the wind was more north-north-westerly. The observed and modeled
 419 potential temperature profiles portray a three-layered structure. Near the surface, a strong
 420 inversion is present in the observed and the modeled data. Above this inversion layer, a
 421 weakly stable residual layer is present up to ≈ 750 m. The free atmosphere with moderately

422 strong stratification is present on top of the residual layer.

423 The observed specific humidity profile shows an interesting multilayer structure: a near-
 424 surface moist layer, a well-mixed residual layer, a drying zone above the residual layer, and
 425 a moist-free atmosphere. The WRF model qualitatively captures this multilayer structure;
 426 however, there is significant room for improvement. The LES-based profile is indistinguish-
 427 able from the WRF profile.

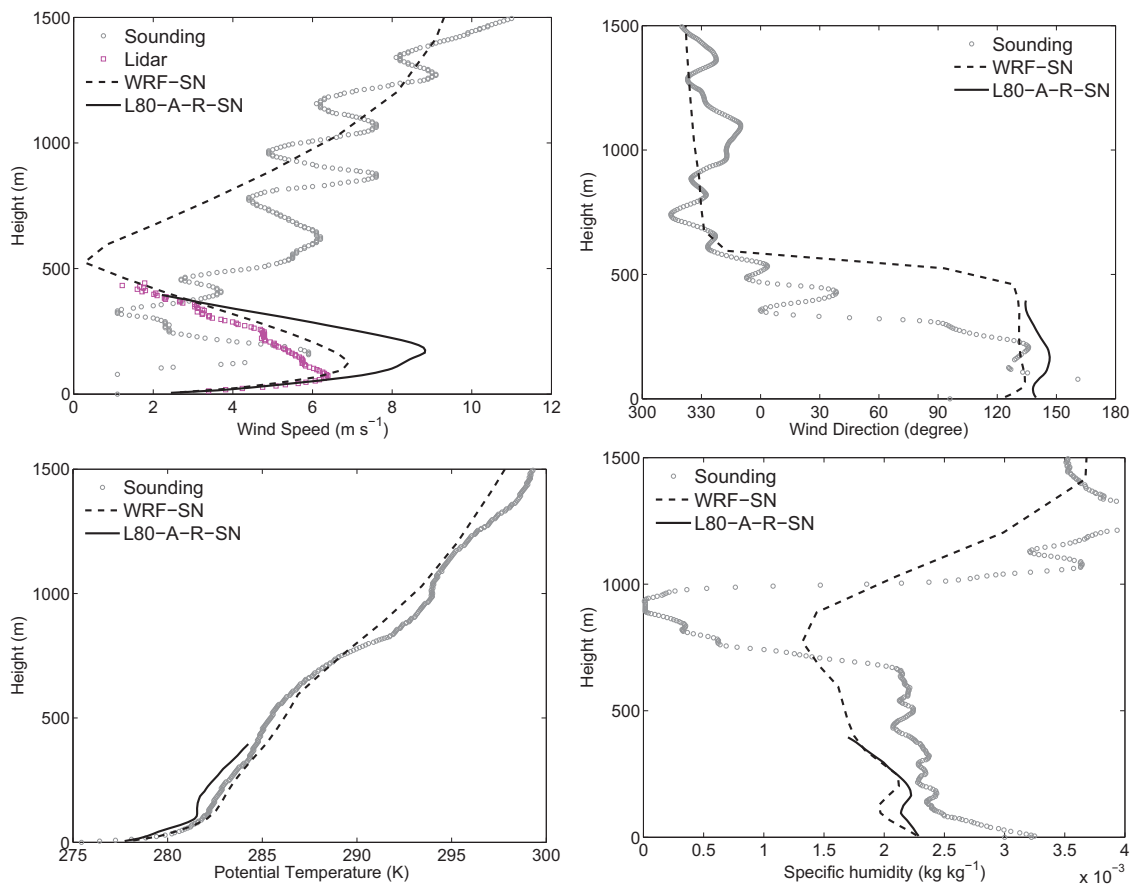


FIG. 13: Plots of the wind speed (top left panel), wind direction (top right panel), potential temperature (bottom left panel), and specific humidity (bottom right panel) profiles corresponding to 11 UTC.

428 Figure 13 shows profiles from 11 UTC. Almost all the remarks made in the context of
 429 Fig. 12 also hold for this figure and, thus, are not repeated. However, we would like to note
 430 that the wind direction in the SBL shifted towards south-south-east at this time due to
 431 inertial oscillation even though the upper layer wind was still from the north-north-westerly
 432 direction.

433 In Fig. 14, we plot hodographs from observational (0-12 UTC) and modeled (5-12 UTC)
 434 data. Since lidar data did not include wind direction information, we utilized sodar and tower
 435 wind data. Note that the tower data were not available after ≈ 8 UTC. The signature of
 436 inertial oscillations^{87,93} is clear in the observed and modeled hodographs. The hodographs
 437 from the mesoscale and LES runs are almost identical—emphasizing, again, the similar
 438 dynamical evolutions.

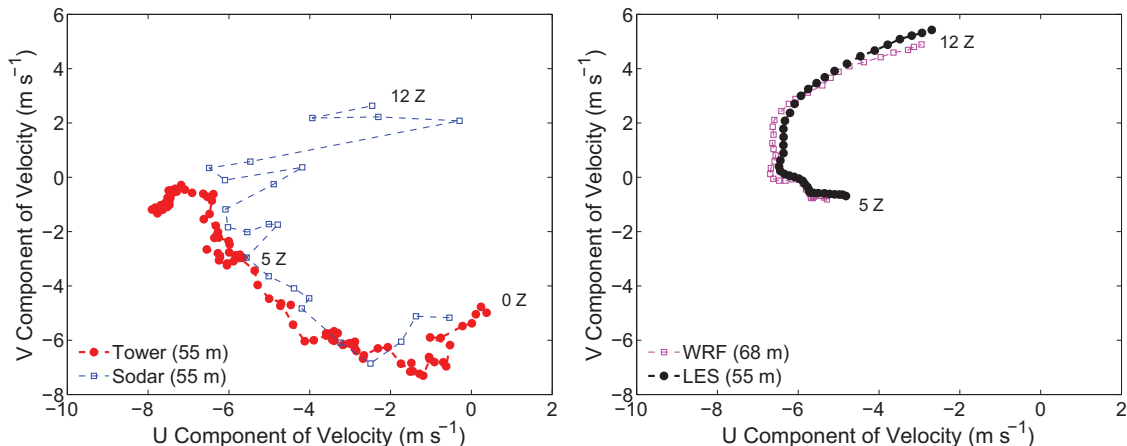


FIG. 14: Observed (left panel) and simulated (right panel) hodographs. In the left panel, the red dots represent velocity observations (with temporal averaging of 5 min) measured by a sonic anemometer located on the 60 m tall meteorological tower (55 m AGL). Wind measurements from a sodar at Beaumont (with temporal averaging of 30 min; 55 m AGL) are plotted as blue squares in the left panel. Simulated data from the WRF model and the MATLES model are represented by magenta dots and black squares, respectively, in the right panel. The signature of inertial oscillations is visible in both the panels.

439 B. Second-Order Statistics

440 Before elaborating on these results, we would like to briefly describe our plotting strategy
 441 for variance and flux profiles from the LES runs. As mentioned before, the LES data were
 442 saved every 10 min. Thus, for every hour, there are 6 data samples corresponding to each
 443 vertical level. From these data points, we calculate and plot the median (p50) values. In
 444 addition, the entire range (minimum to maximum) of the LES values is shown as a shaded
 445 band. The sonic anemometer data from the EOL and WUR towers are available every 5

446 min. Analogous to the LES profiles, we also report the median in conjunction with the
447 minimum and maximum values from these datasets.

448 Observed and simulated variance profiles are shown in Fig. 15. Note that the MATLES
449 model does not solve a prognostic equation of turbulent kinetic energy (TKE); for this reason,
450 we only show the resolved variances from LES. Since EOL tower data are not available after
451 8 UTC, we report results from two consecutive time frames: 6-7 UTC and 7-8 UTC. We
452 did not report turbulence data from 5-6 UTC as this time was considered to be part of the
453 spin-up period for the LES runs.

454 From the modeled variance profiles it is quite clear that the nocturnal turbulence is
455 generated near the surface and transported upwards. A non-traditional upside-down char-
456 acter^{53,66}, where turbulence is generated in the outer SBL rather than at the surface, does
457 not appear in our simulation. In contrast, the horizontal variance observations at 50 and
458 55 m levels, during 6-7 UTC, might indicate the existence of an upside-down SBL.

459 There are some differences between the variances computed from measurements by the
460 EOL and WUR sonic anemometers. These could be the result of small-scale topographi-
461 cal effects (the towers were a few tens of meters away from each other) or they could be
462 attributed to differences in instrumentation and/or in the variance calculation.

463 The observed and modeled horizontal velocity variance and potential temperature vari-
464 ance become very small above ≈ 50 m AGL. This height is much shallower than $h_{LLJ} =$
465 100 m. In idealized LES studies, h estimated from vertical profiles of different variables
466 (e.g., wind speed, wind-speed profile curvature, stream-wise velocity variance, vertical ve-
467 locity variance, momentum flux, buoyancy flux) are usually very similar (e.g.,⁷³). In contrast,
468 in the case of observational data, different profiles can lead to significantly different estimates
469 of h (see^{70,83,96} and the references therein). It was interesting to find out that an LES model
470 with appropriate forcings can also generate different variables with different h values.

471 The magnitude of the simulated horizontal velocity variance is larger than the correspond-
472 ing observed value (especially during 7-8 UTC). This could be due to an inherent limitation
473 of the LES approach, or a result of the omnipresent spatial variability. In Fig. 16, we plot
474 streamwise variance from a doppler lidar. Recently, Pichugina et al.⁶⁹ reported good corre-
475 lation between sonic anemometer and lidar data for weakly stable conditions. However, in
476 the present case, the lidar-based variances are much larger than the sonic anemometer-based
477 variances. In other words, there is tremendous discrepancy between the sonic anemometer-

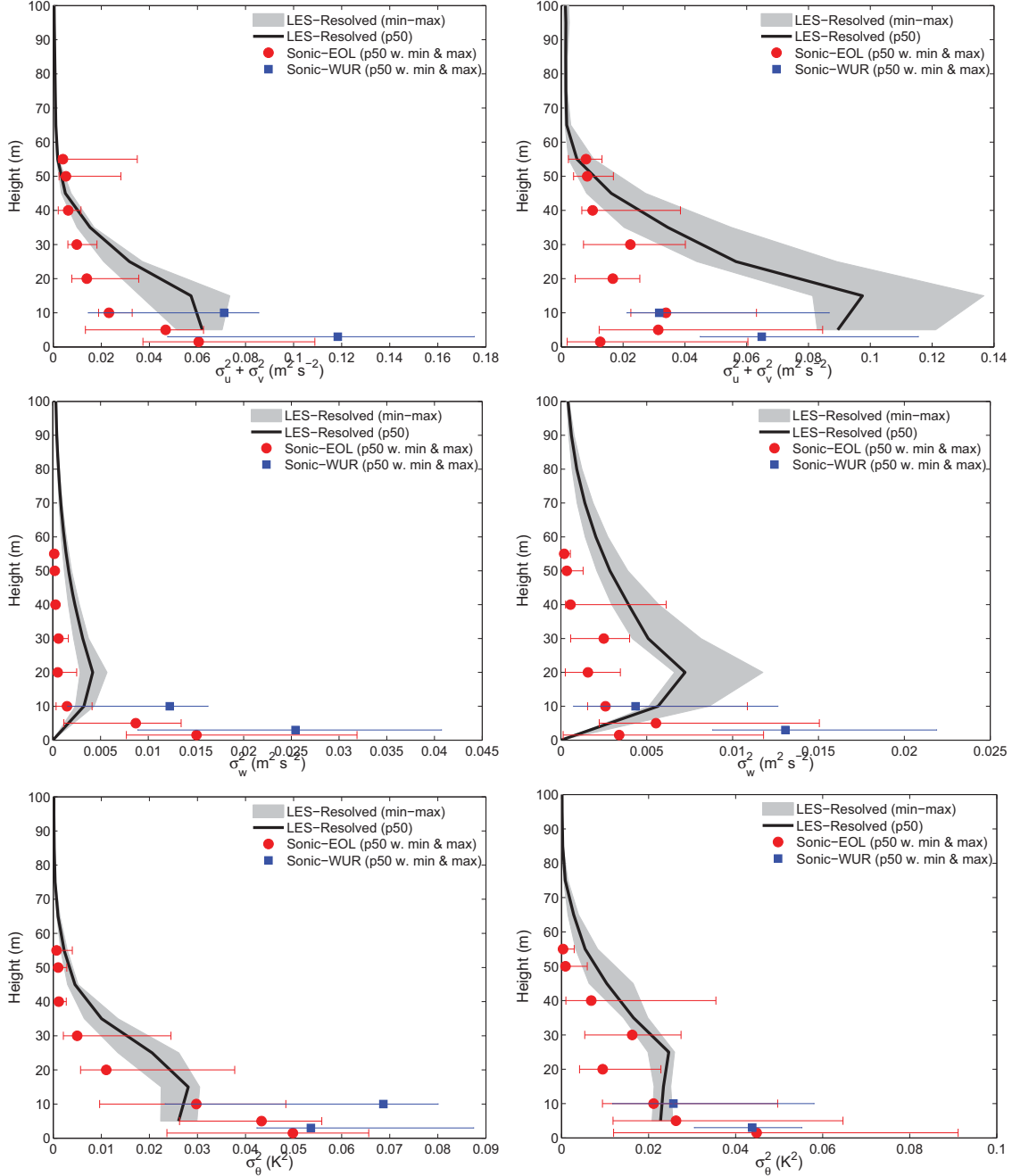


FIG. 15: Plots of variance profiles corresponding to 6–7 UTC (left panels) and 7–8 UTC (right panels). The top, middle, and bottom panels represent horizontal velocity variance ($\sigma_u^2 + \sigma_v^2$), vertical velocity variance (σ_w^2), and potential temperature variance (σ_θ^2), respectively. The red dots with whiskers represent median and minimum-to-maximum values of the observations from the 60 m tall meteorological tower. The solid black lines and the light grey areas correspond to the medians and the minimum-to-maximum ranges, respectively, of the LES-generated output data. Note that the simulated results represent resolved variances, whereas the observed data correspond to total variances.

478 and doppler lidar-based estimates of variances; the LES values are somewhat in between the
 479 two.

480 The LES model underestimates the vertical velocity and temperature variances near the
 481 surface. This is likely due to the lack of spatial resolution. We will revisit this issue later in
 482 this paper.

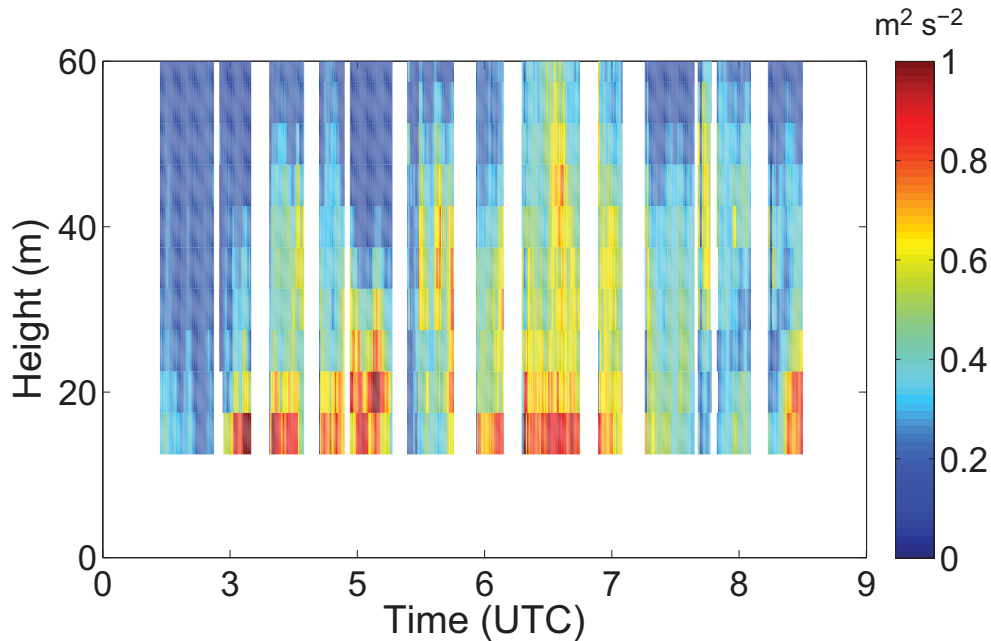


FIG. 16: Time-height plot of doppler lidar-based variances.

483 Vertical profiles of the local friction velocity (u_{*L}), computed using local momentum
 484 fluxes, and the sensible heat flux ($\langle w'\theta' \rangle$) are shown in Fig. 17. In contrast to the variance
 485 plots, in these plots, the total LES-generated fluxes (resolved plus SGS) are shown. In
 486 addition, the resolved fluxes alone are overlaid for comparison.

487 As with the variance plots, there are some differences between the fluxes measured by
 488 the EOL and WUR sonic anemometers. The exact cause for these differences is unknown to
 489 us; however, we can speculate and ‘blame’ the differences on small-scale topographic effects,
 490 instrumentation, and/or flux calculations.

491 Even though the LES captures the near-surface observed fluxes during 6-7 UTC, it over-
 492 estimates them at higher levels and also during 7-8 UTC. The resolved component of the
 493 fluxes is much smaller than that of the corresponding SGS fluxes. For a moderately/strongly
 494 stratified case, this behavior is expected from an LES run using a grid resolution of 10 m.

495 A finer grid resolution will undoubtedly lead to a larger contribution of resolved fluxes; it
496 might also reduce the spurious pile-up of momentum fluxes above 50 m AGL. However,
497 a finer grid resolution is not expected to change the total flux profiles in any substantial
498 manner; we will provide supporting evidence later in this paper.

499 The modeled variance and flux profiles are consistent with each other—they both reduce
500 to zero or small residual values above ≈ 50 m AGL. However, the observed variance and
501 flux profiles behave differently. The behavior of the observed sensible heat flux is especially
502 intriguing—it vanishes almost completely above 20 m AGL. It is, thus, no surprise that
503 Vickers and Mahrt⁹⁶ reported h to be barely 20 m at 4 UTC, based on similar buoyancy
504 flux profiles. It is not clear to us whether, by simply refining grid resolution, the LES model
505 will be able to capture this behavior. We will attempt to resolve this issue in future work.

506 C. Temporal Evolution

507 The night of October 23/24 was classified as an intermittent turbulent night by van
508 de Wiel et al.⁹⁴. In this section, we investigate whether the coupled mesoscale-large-eddy
509 modeling approach managed to capture this intermittency in turbulence. We utilized two
510 types of turbulent flux measurements for model validation.

511 Traditionally, sonic anemometry (also known as the eddy-covariance approach) is used
512 for measuring turbulent fluxes²⁹. Recent micrometeorological studies^{26,32,55,56} have demon-
513 strated, however, that the use of scintillometry is a viable alternative to sonic anemome-
514 try. A scintillometer consists of a transmitter and a receiver and employs the principle of
515 ‘scintillation’—turbulence-induced fluctuations of the observed intensity of a remote light
516 source. Over the years, different types of scintillometers have been developed using different
517 wavelengths, aperture sizes, and configurations (see the reviews by² and³³ for more informa-
518 tion). With a small-aperture scintillometer (SAS), one can estimate the structure parameter
519 of the refractive index, C_n^2 , and the inner scale of turbulence, l_0 , from measured amplitude
520 fluctuations. Note that C_n^2 and l_0 are directly related to the temperature structure param-
521 eter, C_T^2 , and the kinetic energy dissipation rate, ϵ . By using Monin-Obukhov similarity
522 theory, one can extract momentum and sensible heat fluxes from C_T^2 and ϵ .

523 During the CASES-99 field campaign, researchers from Wageningen University (WUR),
524 the Netherlands, deployed a displaced-beam SAS instrument (SLS20 by Scintec). The trans-

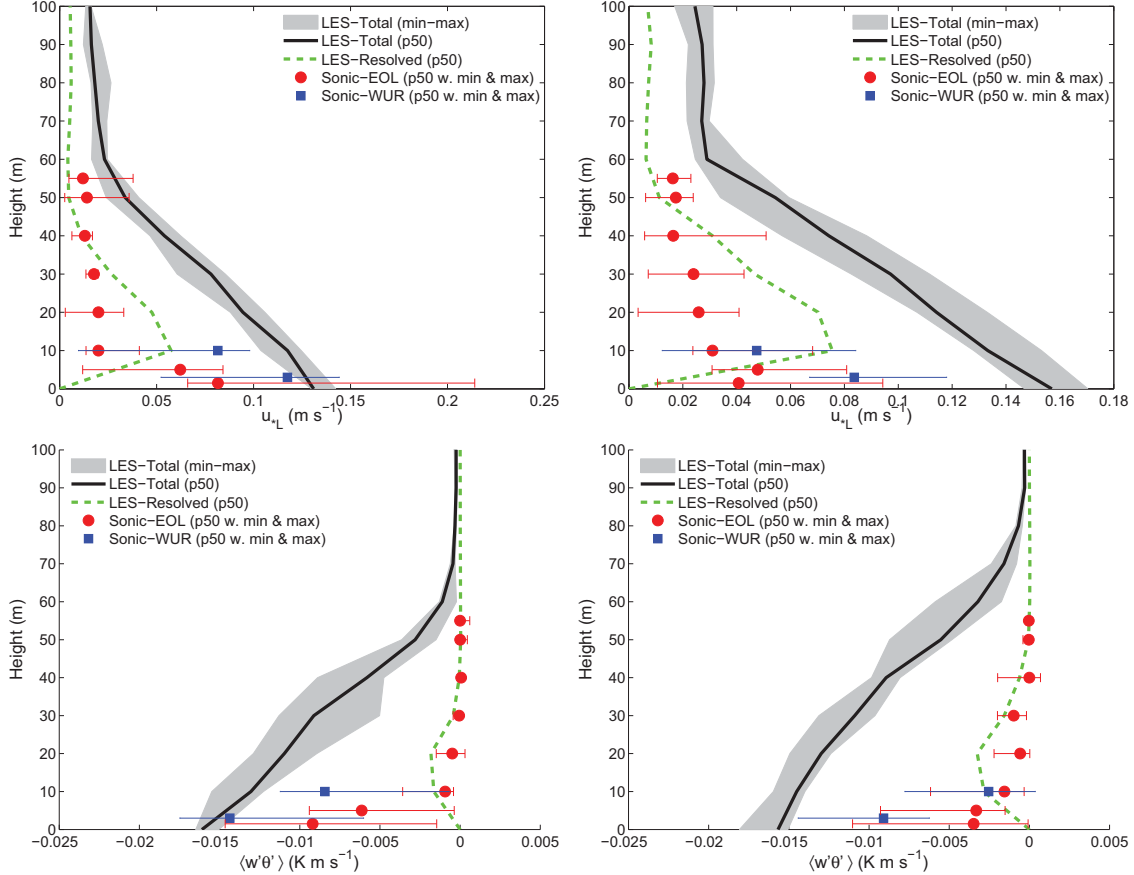


FIG. 17: Plots of local friction velocity (top panels) and sensible heat flux (bottom panels) profiles corresponding to 6–7 UTC (left panels) and 7–8 UTC (right panels). The red dots with whiskers represent median and minimum-to-maximum values of the observations from the 60 m tall meteorological tower. The solid black lines and the light grey areas correspond to the medians and minimum-to-maximum ranges of the LES-generated output data, respectively.

mitter and receiver were installed at 2.46 m AGL. The path length between the transmitter
 and the receiver was 112 m. Please refer to Hartogensis et al.³² for more information on the
 SAS experimental setup.

In contrast with conventional sonic anemometers, a SAS requires short averaging intervals
 (because spatial averaging over a line of sight relaxes the need for long temporal averaging)
 and is expected to respond rather quickly to changing (non-stationary) atmospheric con-
 ditions. During the CASES-99 field campaign, a sampling interval of 6 s was used by the
 WUR team³².

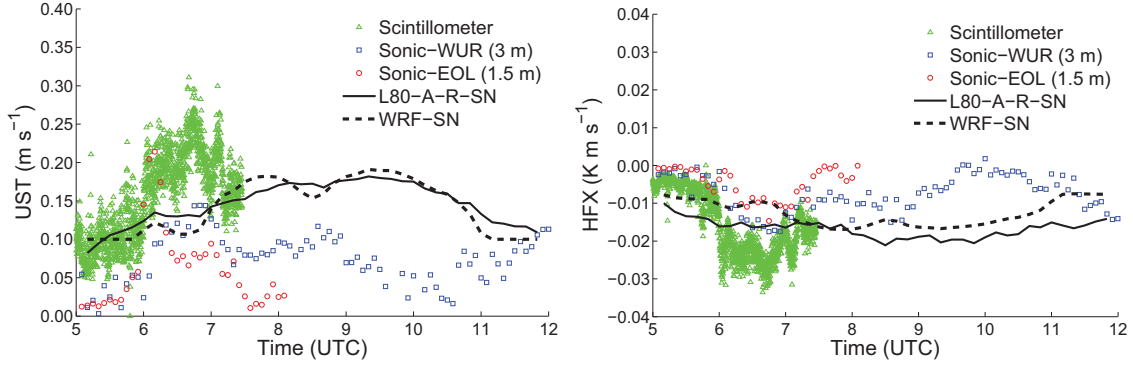


FIG. 18: Time series of surface friction velocity (left panel) and sensible heat flux (right panel). Fluxes measured by a small-aperture scintillometer are depicted with green triangles. Observations from sonic anemometers at 1.5 m and 3 m AGL are represented by stars and circles, respectively. The solid blue and red lines denote the output from the WRF model and the MATLES model, respectively. The observed fluxes clearly portray intermittent behavior.

533 In Fig. 18, the observed and modeled surface fluxes are shown. Surprisingly, the SAS-
 534 based fluxes were significantly larger in magnitude than the sonic anemometer-based fluxes;
 535 more interestingly, they were even larger than the modeled fluxes. It is possible that the
 536 scintillometer faithfully captured the spatial variability of nighttime surface fluxes. In that
 537 case, the SAS-based fluxes (representing path-averaged fluxes) are more realistic than the
 538 sonic anemometer-based fluxes (representing point observations). Another possibility is
 539 that the Monin-Obukhov similarity functions utilized by the scintillometer are problematic
 540 in the intermittent turbulence regime. If that is the case, then the SAS-based fluxes are not
 541 trustworthy. More research is definitely needed in this scientific arena.

542 The observed surface fluxes clearly show signs of intermittency. In contrast, the WRF-
 543 and MATLES-generated fluxes are more or less continuous in time. The YSU surface layer
 544 scheme of the WRF model artificially clips u_* at 0.1 m s^{-1} to avoid the so-called runaway
 545 cooling problem. This spurious behavior is clearly visible in the left panel of Fig. 18. Given
 546 that during 6-11 UTC, the WRF-based friction velocity (u_*) is much higher than 0.1 m s^{-1} ,
 547 we believe that the clipping has not impacted our results in any significant manner. Never-
 548 theless, in our future work, we will study the impact of this clipping and other thresholding
 549 operations on the simulation of intermittent turbulence.

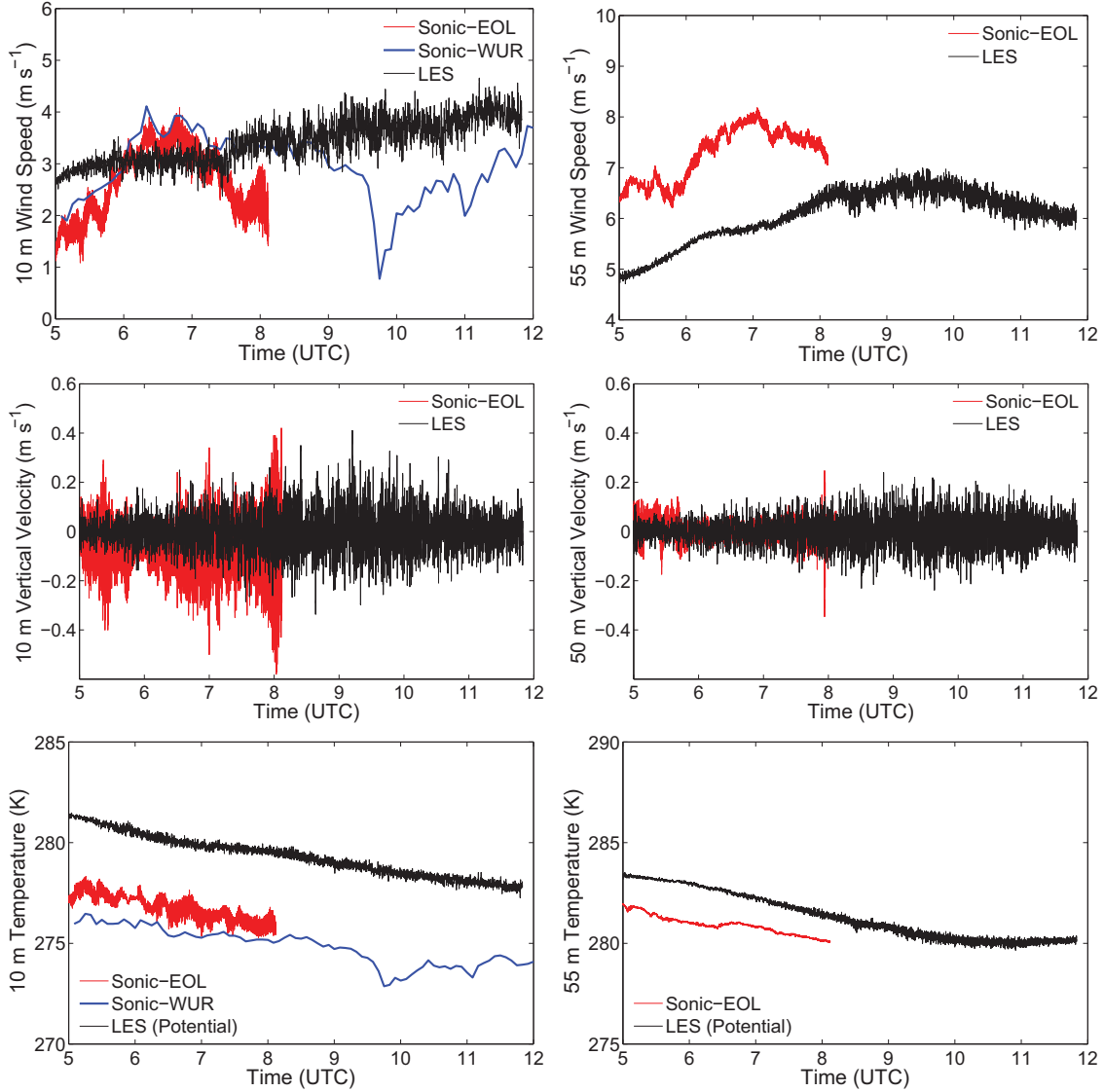


FIG. 19: Time series of wind speed (top panels), vertical velocity (middle panels), and temperature (bottom panels). The left and right panels correspond, respectively, to the near-surface layer (10 m) and the outer layer (55 m for wind speed and temperature; 50 m for vertical velocity).

550 The WRF-simulated results are in complete agreement with those reported by Shin
 551 and Hong⁷⁷. All of their WRF simulations (without exception) utilizing various PBL and
 552 SL schemes overestimated nighttime (u_*) values when compared against observed sonic
 553 anemometer data. At 5 UTC, their simulated u_* values were in the range, 0.15-0.2 m s⁻¹.
 554 By the end of their simulations (i.e., at 12 UTC), the u_* values decreased to approximately

555 0.10-0.15 m s⁻¹. Similarly, all the WRF simulations also overestimated the magnitude of
556 (downward) sensible heat flux ($\langle w'\theta' \rangle$) values. The simulated $\langle w'\theta' \rangle$ values remained more
557 or less constant during the period of 5-12 UTC. Shin and Hong⁷⁷ pointed out that the sim-
558 ulated nighttime surface variables were quite convergent. In fact, the standard deviation for
559 the different simulations was only 0.01 m/s for friction velocity; they were on the order of
560 4-5 W m⁻² in the case of sensible heat flux (see Table 2 of⁷⁷).

561 In Fig. 19, we plot time series of observed and LES-generated horizontal wind speed,
562 vertical velocity, and temperature. In the case of LES, the time series represent simulated
563 data (sampling rate, 10 Hz) from a grid point at the center of the model domain. As noted
564 before, sonic anemometer data from EOL (frequency, 20 Hz) were not available after \approx
565 8 UTC. Hence, for model validation, we also plotted the 5-minute-averaged data from the
566 WUR sonic anemometer.

567 For most of the variables, the LES qualitatively captured the range of fluctuations; how-
568 ever, the trends were notably different from the observations. A temporal shift of 3 h is
569 evident in the upper-level (55 m) horizontal wind speed data (see the discussion earlier in
570 the context of inertial oscillation).

571 Both the observed horizontal wind speed and the vertical velocity display non-stationary
572 character. The LES-generated time series show qualitatively similar behavior; the non-
573 stationary character captured in the simulations is attributed to use of realistic boundary
574 and forcing conditions. For example, soon after the intensification of the simulated LLJ
575 (around 8 UTC), the wind speed fluctuations increased significantly due to shear-generated
576 turbulence (top panels of Fig. 19). The observed vertical velocity time series show some
577 evidence of intermittency. Unfortunately, such intermittency patterns were not present in
578 the LES-generated data.

579 The near-surface (10 m) observed temperature and horizontal wind speed data show some
580 periodic oscillations. Similar oscillations were lacking in the modeled (potential) temperature
581 and wind speed data. Results reported by Steeneveld et al.⁸² and Shin and Hong⁷⁷ also did
582 not show any oscillations. According to Revelle⁷² and van de Wiel⁹², these oscillations are
583 strongly coupled to the phenomenon of surface flux intermittency. Clearly, the mesoscale
584 and large-eddy models are deficient in this regard.

585 A few minutes before 10 UTC, the WUR sonic anemometer data show signs of the
586 runaway cooling phenomenon. Based on Figs. 18 and 19, we see evidence in the observations

587 of: (i) decoupling of the atmospheric boundary layer from the underlying surface (sharp
588 decrease in the near-surface wind speed; turbulent fluxes become negligible); and (ii) rapid
589 cooling of the near-surface air temperature. The WRF and MATLES models were unable
590 to capture these features.

591 D. Spectral Analysis

592 Traditionally, wavenumber spectra are utilized to assess the strengths and weaknesses
593 of LES-SGS models. It is well documented that non-dynamic (i.e., static) SGS models
594 are over-dissipative as indicated by steeper spectral slopes at higher wavenumbers. On the
595 other hand, in the case of the dynamic SGS models (such as the LASDD SGS model), the
596 longitudinal velocity and scalar spectra clearly show extended inertial ranges (see^{1,12} for
597 examples). To the best of our knowledge, the characteristics of LES-generated spectra at
598 larger scales (e.g., the mesoscale, the terra-incognita regime described by⁹⁷) are not discussed
599 in the literature.

600 A few years ago, Muschinski et al.⁶¹ analyzed observational data from the CASES-99
601 field campaign. They utilized high-resolution (200 Hz) turbulence data from the CIRES
602 Tethered Lifting System (52–74 m AGL). Their frequency-domain spectra showed three dis-
603 tinct regimes (see bottom right panel of Fig. 20): an inertial range (slope $\approx -5/3$), a spectral
604 gap (slope ≈ 0), and a mesoscale range (slope $\approx -5/3$). It was interesting to assess how our
605 coupled mesoscale-LES approach captured these scaling regimes. We used sonic anemome-
606 ter data, collected by NCAR-EOL for comparison. Since the observed and modeled time
607 series were non-stationary, we used a discrete wavelet transform (Haar wavelet) approach
608 to compute the frequency-domain spectra. A similar approach was used by Katul et al.⁴³
609 and Basu et al.⁹. Results are presented in Fig. 20 and are quite intriguing. The following
610 comments can be made based on this figure:

- 611 • The sonic anemometer-based horizontal wind speed and temperature spectra portray
612 slopes of -3 in the mesoscale regime; this is a hallmark of two-dimensional turbulence⁴⁸.
613 In strongly stratified conditions, due to the lack of vertical diffusion, eddies can become
614 quasi-two-dimensional (pancake-shaped); in such cases, one would intuitively expect a
615 -3 slope in the spectra. Since Muschinski et al.⁶¹ analyzed data from a different night,

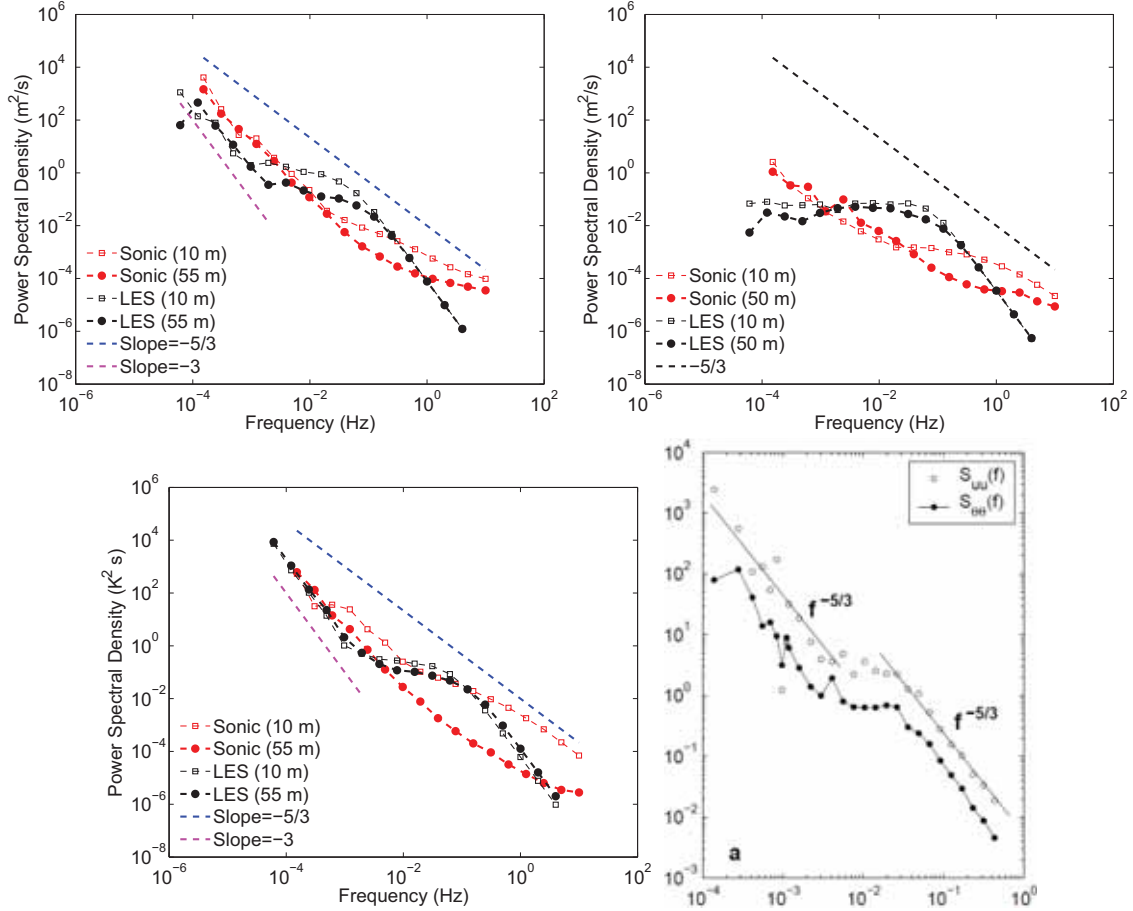


FIG. 20: Wavelet spectra of horizontal wind speed (top left panel), vertical velocity (top right panel) and temperature (bottom left panel). For comparison, spectra reported by Muschinski et al.⁶¹ are shown in the bottom right panel (units are $\text{m}^2 \text{s}^{-2} \text{Hz}^{-1}$ for $S_{uu}(f)$ and units, corrected relative to ⁶¹, are $\text{K}^2 \text{Hz}^{-1}$ for $S_{\theta\theta}(f)$). Spectral gaps (around 0.01 Hz) are noticeable in the spectra for wind speed and temperature.

616 it is quite possible that they captured a weakly stable regime with three-dimensional
 617 motions.

618 • In agreement with the observational spectra, in the case of horizontal wind speed and
 619 temperature, the modeled mesoscale spectra also show slopes of -3. This specific result
 620 significantly boosts our confidence in the simulated data.

621 • For the high-frequency (inertial) range, most of the sonic anemometer data-based spec-
 622 tra become flat; this is perhaps due to measurement noise. In very stable conditions,

623 sonic anemometers can suffer from several types of instrumental and sampling prob-
624 lems (e.g., dropouts, insufficient amplitude resolution)—please refer to Vickers and
625 Mahrt⁹⁵ for further discussion on this topic.

626 • The LES-generated spectra show steeper than $-5/3$ slopes in the inertial range. This
627 discrepancy in the inertial range is expected to reduce with increased spatial resolution;
628 however, such simulations would be computationally quite expensive. As a viable
629 alternative, for engineering applications, a fractal interpolation approach could be
630 used to recover the energy in this range (see^{9,78} for details).

631 • The location of the modeled spectral gap (around 0.01 Hz) is identical with the results
632 reported by Muschinski et al.⁶¹. In the case of the sonic anemometer data, the spectral
633 gaps are somewhat discernible for the near-surface vertical velocity and the tempera-
634 ture data. Note that the existence of a spectral gap around 0.01 Hz was also reported
635 earlier by Caughey²². This information was used by several researchers (e.g.,^{10,63}) to
636 partition mesoscale and turbulent motions prior to flux estimation.

637 • The observed vertical velocity spectra appear to follow a $-5/3$ scaling. In contrast, the
638 modeled vertical velocity spectra display a flattening behavior in the low-frequency
639 range. We speculate that, by increasing the model domain size, we might improve the
640 shape of these spectra.

641 E. Sensitivity Experiments

642 In this section, we report results from various sensitivity experiments.

643 1. *Observational Data Assimilation*

644 As mentioned in Section VI, in this work, we performed two mesoscale simulations. One
645 of these simulations, called WRF-SN, included four-dimensional data assimilation (FDDA)
646 of public-domain observations; the other simulation, called WRF-NN, did not include such
647 data assimilation. In Fig. 21, we present results from the WRF-NN simulation. We also
648 show differences between this simulation and the WRF-SN simulation. It is evident that
649 differences between the WRF-SN and WRF-NN simulations are quite small. This result was

650 not unexpected; since the NARR dataset included a significant amount of observational data,
651 the impact of additional observational data was not significant. However, if one uses other
652 data products with less assimilated data (e.g., NCEP/NCAR Global Reanalysis Project,
653 2.5-degree resolution, every 6 hours; NCEP GDAS FNL Analysis, 1-degree resolution, every
654 6 hours; NCEP Eta/NAM AWIP, 40-km resolution, every 6 hours), we would anticipate
655 significantly greater (positive) impact of the use of FDDA in the WRF simulations.

656 2. *Grid Resolution*

657 In addition to the LES runs with $80 \times 80 \times 80$ grid points, we performed two additional
658 runs: L64-A-RR-SN, with $64 \times 64 \times 64$ grid points and L40-A-R-SN, with $40 \times 40 \times 40$ grid
659 points. Results from these runs are presented in Figs. 22–24. The following inferences can
660 be made based on these figures and Figs. 11, 15, and 17:

- 661 • The simulated mean profiles are almost insensitive to grid resolution. This is a strength
662 of the LASDD-SGS model and has been reported earlier by Basu and Porté-Agel⁸ and
663 Basu et al.¹².
- 664 • The strength of the LLJ peak slightly intensifies with increased resolution.
- 665 • The resolved variances increase with increasing resolution, as would be expected. How-
666 ever, the difference in the resolved variance is small between the L64-A-R-SN and
667 L80-A-R-SN runs (comparing Fig. 23, right panels, with Fig. 15, right panels). This
668 suggests that the resolved variance may not increase significantly with further en-
669 hancement of the grid resolution.
- 670 • Inside the boundary layer, the total momentum flux (represented by the local friction
671 velocity) is almost insensitive to grid resolution. However, above the boundary layer,
672 increased resolution helps in dissipating the pile-up of spurious turbulent fluxes.
- 673 • The total sensible heat flux values are somewhat sensitive to grid resolution. The
674 surface sensible heat flux values during 7–8 UTC change by $\approx 25\%$ by changing the
675 resolution from 20 m to 10 m (comparing Fig. 24, bottom left panel, with Fig. 17,
676 bottom right panel). Similar levels of sensitivity of surface sensible heat fluxes to

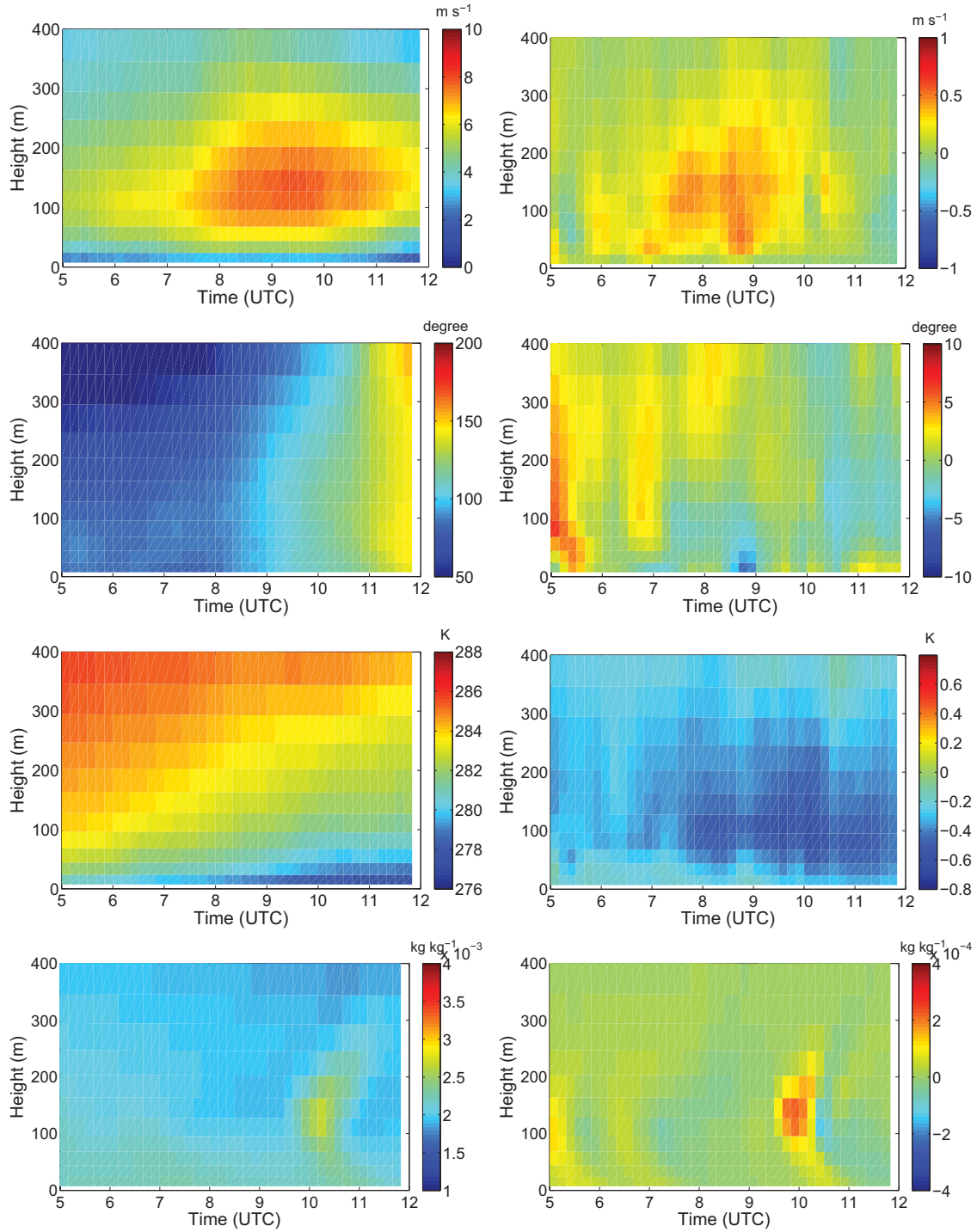


FIG. 21: In the left panel, time-height plots of the WRF model-simulated (domain 4) wind speed (top panel), wind direction (second panel), potential temperature (third panel), and specific humidity (bottom panel) are shown. During this simulation (referred to as the NN simulation), no observational data are assimilated. The right panels show differences between the NN simulation and the control WRF simulation with data assimilation (i.e., NN minus SN).

677 grid resolution were reported by Richardson et al.⁷³ in the context of idealized SBL
678 simulations.

- 679 • As expected, the contribution of the resolved fluxes to the total fluxes increases with
680 increasing resolution. In the L40-A-R-SN run (Fig. 24, bottom right), the resolved
681 sensible heat flux is almost negligible. However, the simulation does not laminarize;
682 the dynamic SGS model essentially acts as a RANS closure in this scenario.

683 **3. Longwave Radiation**

684 In this sub-section, we document the effects of longwave radiation on the LES-generated
685 data. In Fig. 25, results from an LES run with radiation scheme turned off (called L80-A-SN)
686 are presented. In this figure, we also show differences between this simulation and the control
687 simulation (i.e., L80-A-SN minus L80-A-R-SN). The presence of longwave radiational cooling
688 results in a marginally cooler boundary layer and free atmosphere. Near the surface, due
689 to lack of adequate vertical resolution, a small amount of erroneous warming is noticeable.
690 Similar results were reported by Ha and Mahrt³⁰.

691 The overall impact of longwave radiational cooling was insignificant for the other vari-
692 ables. Since the geostrophic wind was moderate (see Fig. 8) during the night of October
693 23/24, radiative flux divergence played a minor role in comparison to turbulent flux diver-
694 gence.

695 **4. Mesoscale Advection**

696 The influence of mesoscale advection forcing is summarized in Fig. 26. In the left panel
697 of this figure, results from the L80-SN run (with no mesoscale advection) are presented. The
698 right panels show differences between this simulation and the control simulation (i.e., L80-
699 SN minus L80-A-R-SN). Since the effects of longwave radiational cooling were found to be
700 marginal, the differences reported in this figure are largely due to the mesoscale advection
701 forcing. The most noteworthy difference is in the height of the stable boundary layer. Due
702 to the lack of thermal advection (see bottom left panel of Fig. 9), the L80-SN run creates
703 a shallower, colder, and more stratified boundary layer in contrast to the L80-A-R-SN run.
704 Due to this stronger stratification, the decoupling of upper air from the surface was stronger

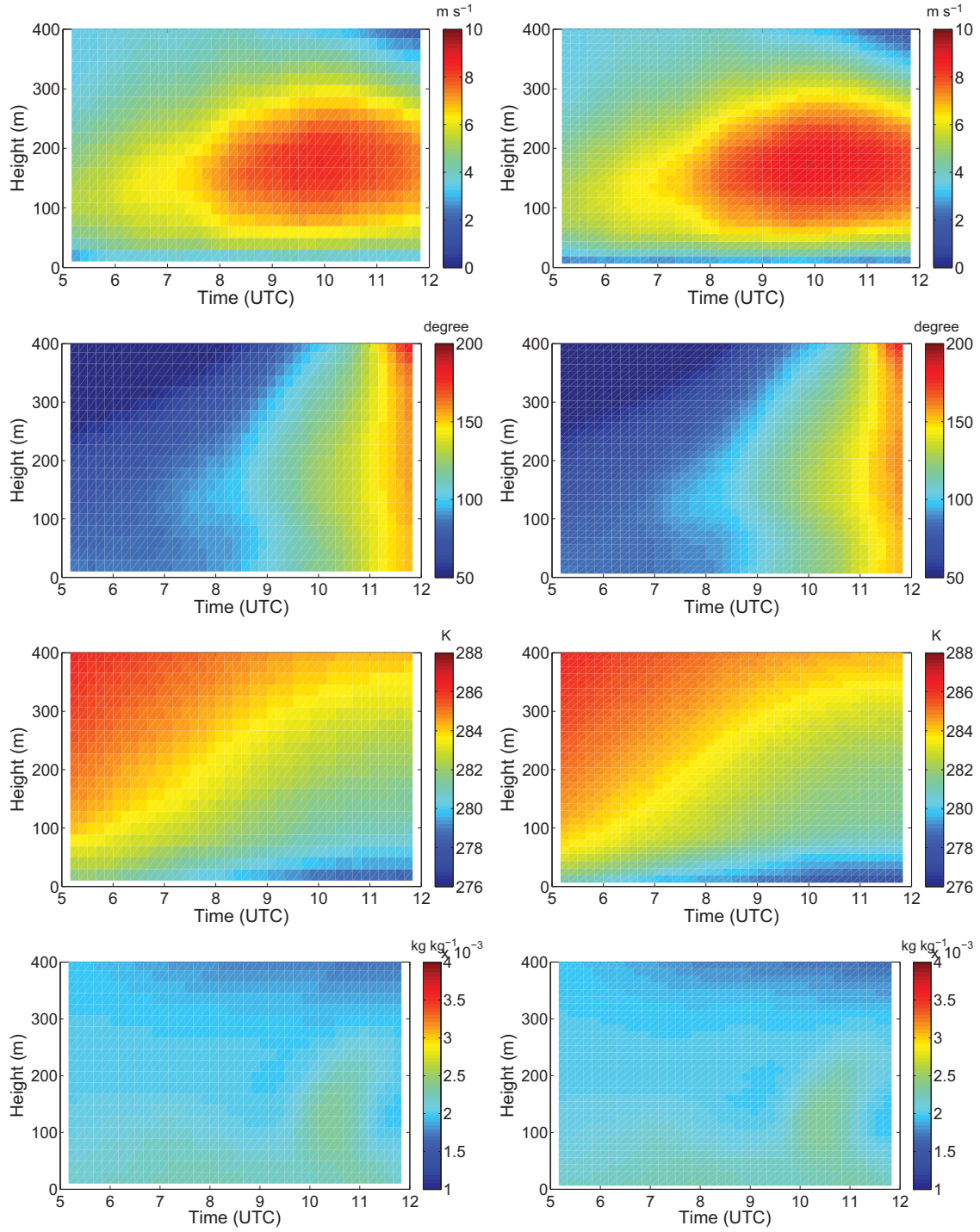


FIG. 22: Time-height plots of simulated wind speed (top panels), wind direction (second panels), potential temperature (third panels), and specific humidity (bottom panels). The left and right panels summarize results from the MATLES model using $40 \times 40 \times 40$ and $64 \times 64 \times 64$ grid points, respectively.

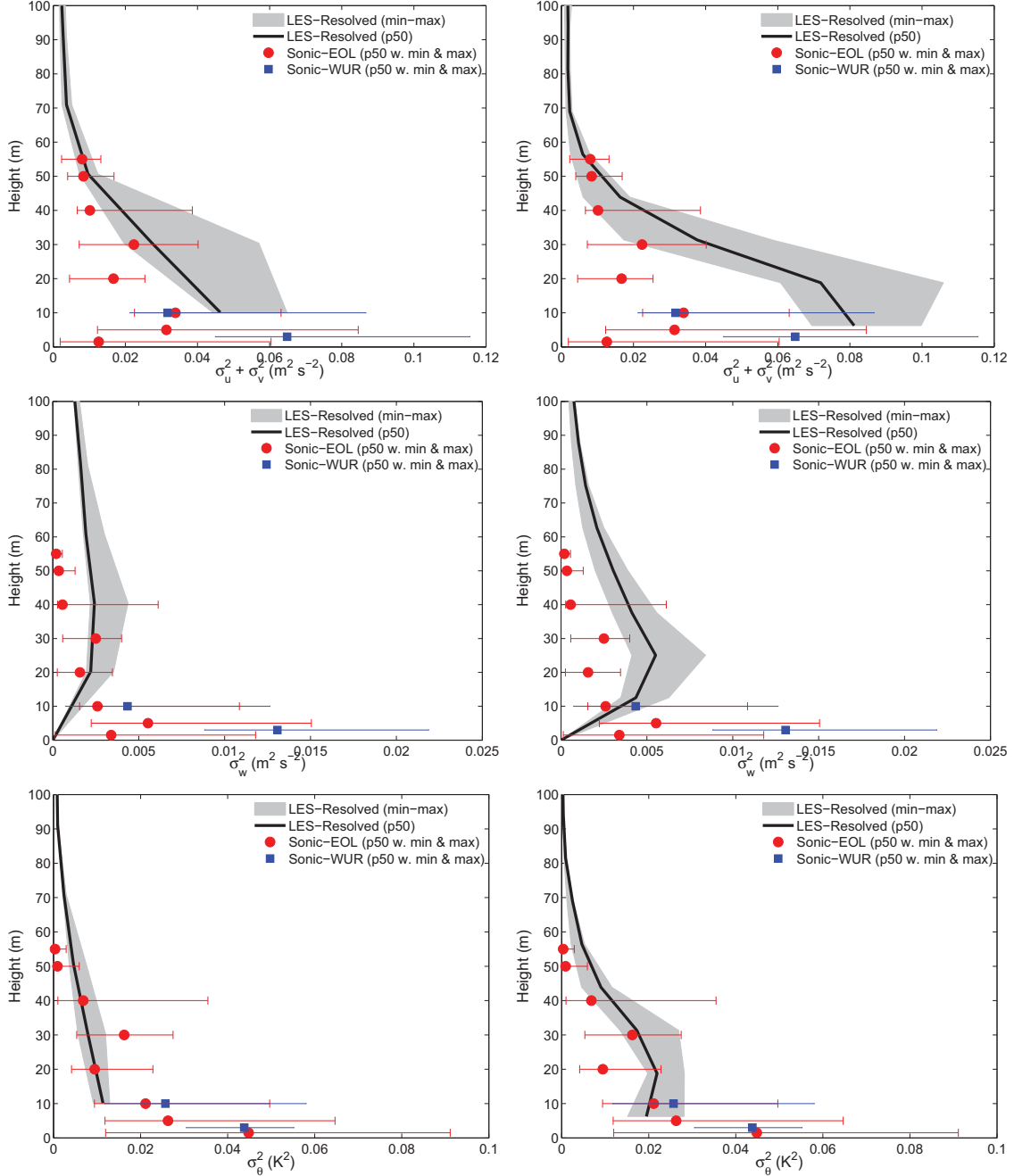


FIG. 23: Plots of variance profiles from the L40-A-R-SN (left panels) and L64-A-R-SN (right panels) runs for 7–8 UTC. The top, middle, and bottom panels represent horizontal velocity variance ($\sigma_u^2 + \sigma_v^2$), vertical velocity variance (σ_w^2), and potential temperature variance (σ_θ^2), respectively. The red dots with whiskers represent median and minimum-to-maximum values of the observations from the 60 m tall meteorological tower. The solid black lines and the light grey areas correspond to the medians and the minimum-to-maximum ranges, of the LES-generated output data. Note that the simulated results represent resolved variances, whereas the observed data correspond to total variances.

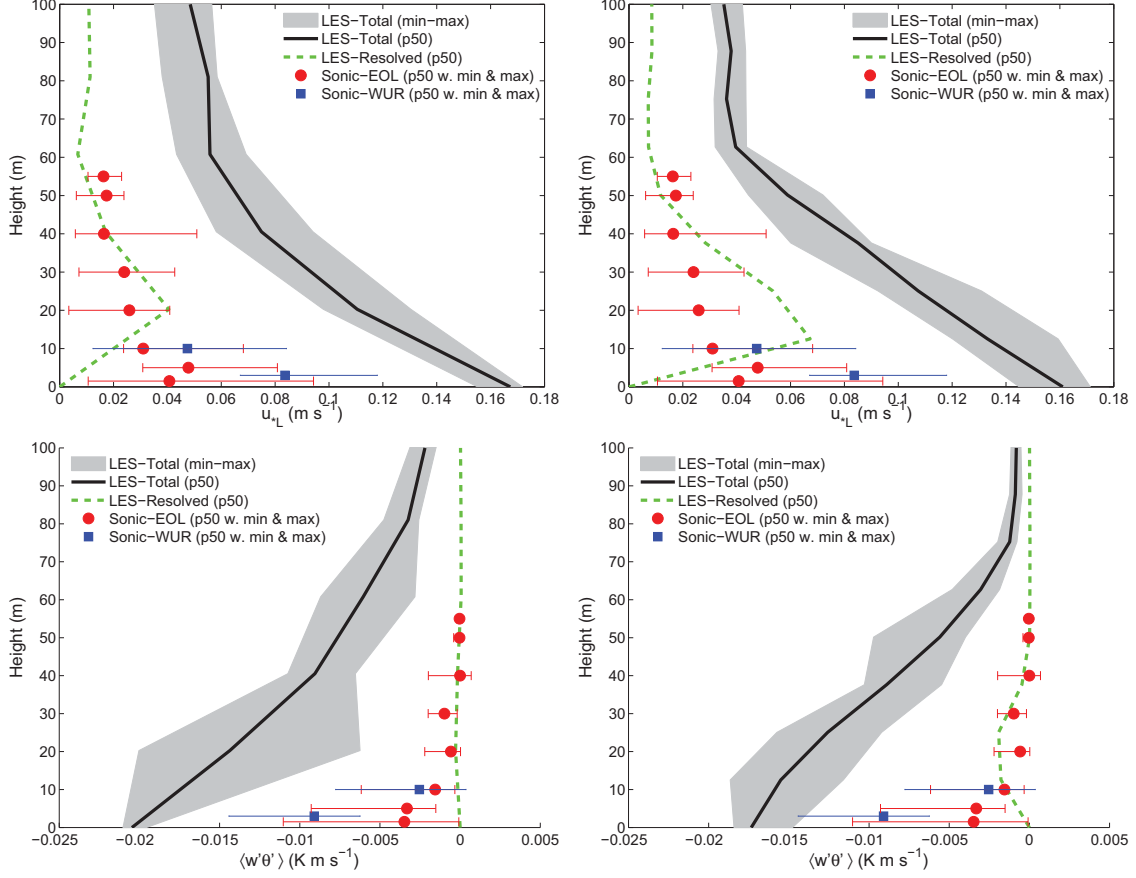


FIG. 24: Plots of local friction velocity (top panels) and sensible heat flux (bottom panels) from the L40-A-R-SN (left panels) and L64-A-R-SN (right panels) runs for 7–8 UTC. The red dots with whiskers represent median and minimum-to-maximum values of the observations from the 60 m tall meteorological tower. The solid black lines and the light grey areas correspond to the medians and minimum-to-maximum ranges of the LES-generated output data, respectively.

705 than in the control case. This decoupling led to a stronger LLJ, which persisted for much
 706 longer than in the control run (Fig. 26).

707 IX. CONCLUDING REMARKS

708 In this study, we proposed a new coupled mesoscale-large-eddy modeling framework.
 709 We demonstrated that if accurate boundary conditions and forcing terms (extracted from a
 710 mesoscale simulation) are used, it is possible for a large-eddy simulation to ‘mimic’ mesoscale

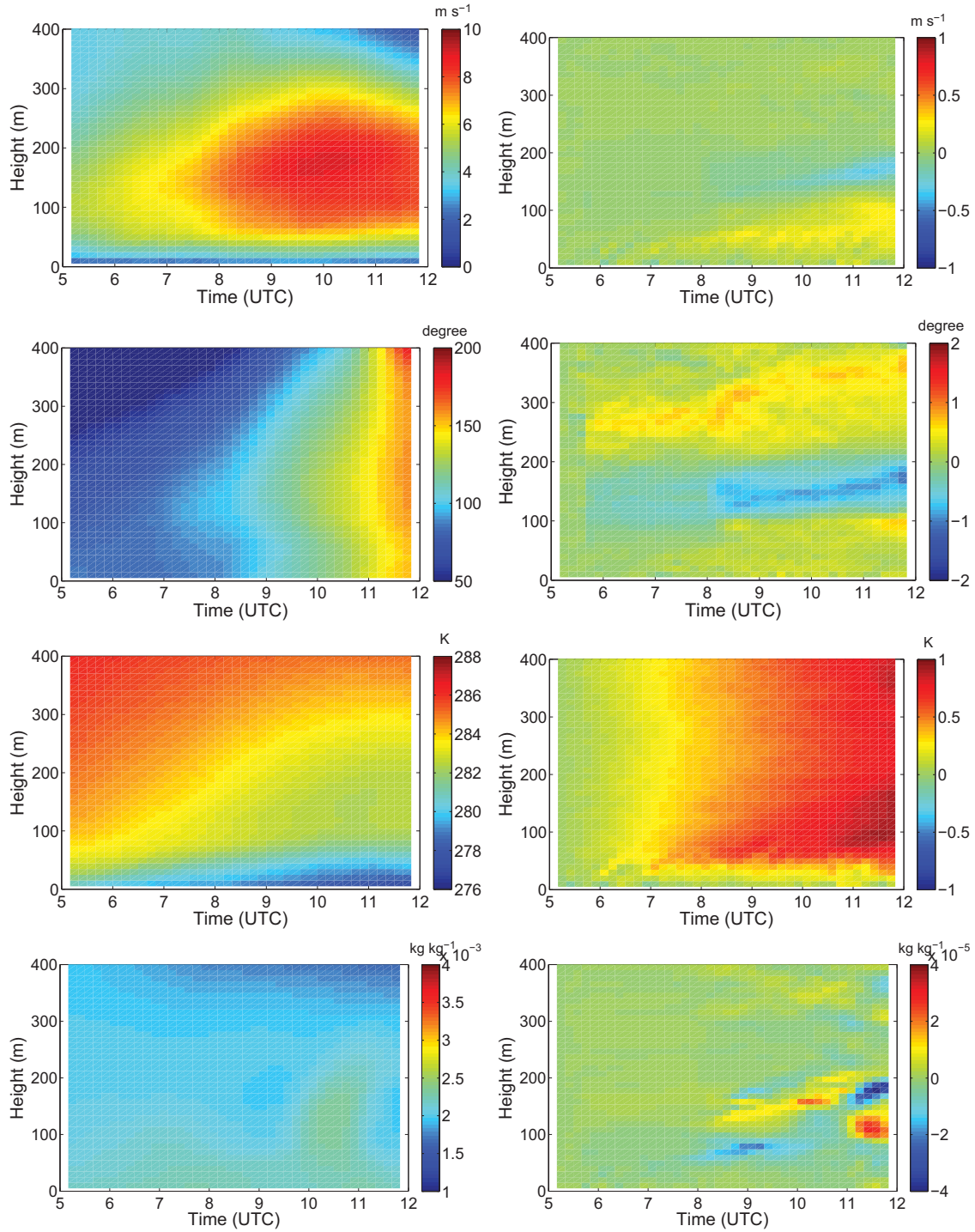


FIG. 25: In the left panels, time-height plots of the MATLES model-simulated wind speed (top panel), wind direction (second panel), potential temperature (third panel), and specific humidity (bottom panel) are shown. The radiation scheme is switched off during this simulation (referred to as L80-A-SN). The right panels summarize differences between this simulation and the control simulation (i.e., L80-A-SN minus L80-A-R-SN).

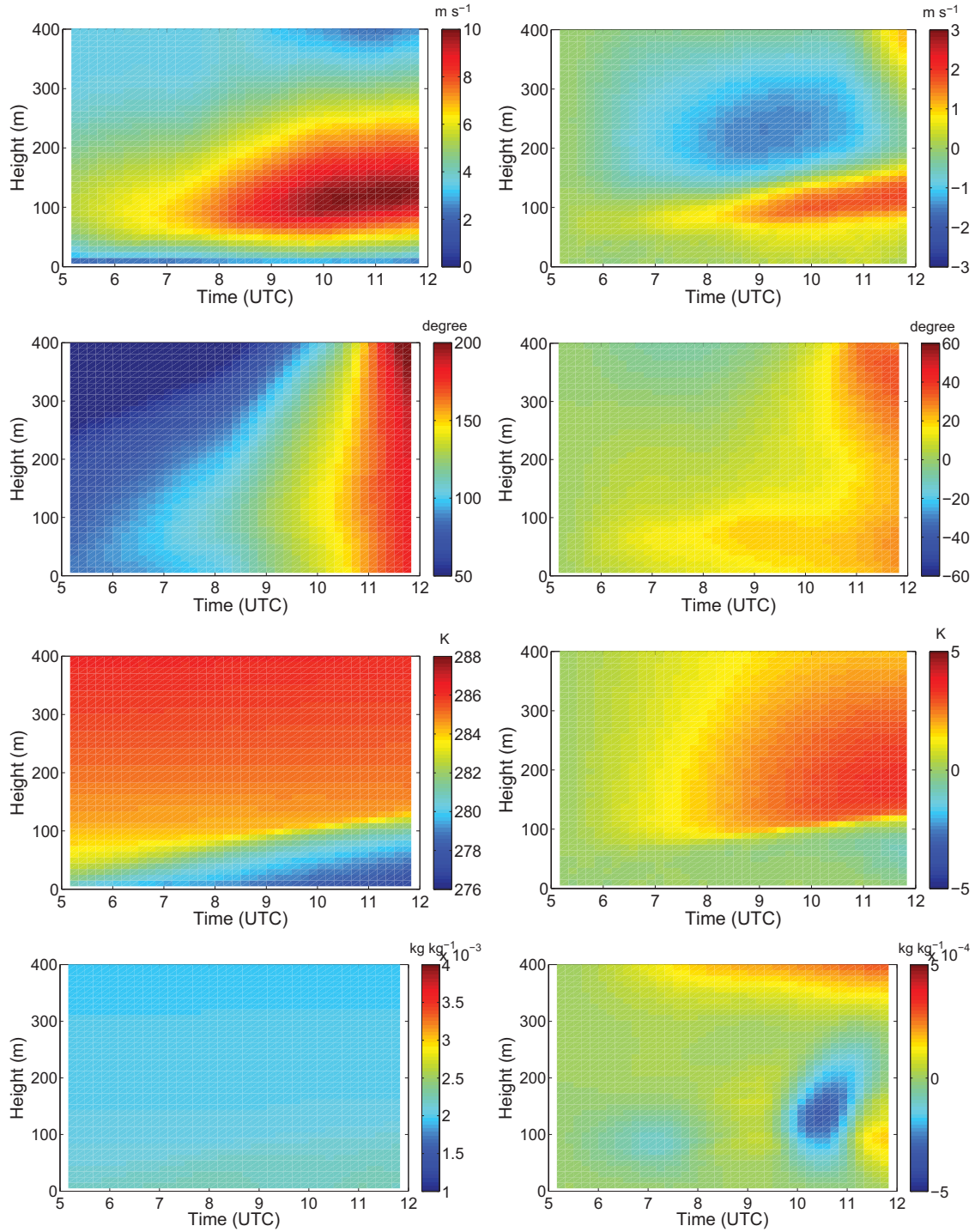


FIG. 26: In the left panels, time-height plots of the MATLES model-simulated wind speed (top panel), wind direction (second panel), potential temperature (third panel), and specific humidity (bottom panel) are shown. During this simulation, the radiation scheme is switched off; also, no mesoscale advection terms are invoked during this simulation (referred to as L80-SN). The right panels summarize difference between this simulation and the control simulation (i.e., L80-SN minus L80-A-R-SN).

711 model-generated first-order statistics (e.g., hodographs). In this manner, we circumvented
712 any ad-hoc nudging of the LES-generated flow fields.

713 The coupled models generated a site-specific realistic stable boundary layer and associated
714 turbulence fields. They reproduced some of the characteristics of an observed low-level jet;
715 the strength of the LLJ, however, was better captured by the LES model than its mesoscale
716 counterpart. More importantly, the LES model, driven by the mesoscale model-generated
717 data, captured different scaling regimes of the energy spectra including the so-called spectral
718 gap. This was one of the key achievements of this study. On the other hand, a major
719 shortcoming of this study is that the coupled models were unable to capture the intermittent
720 nature of the observed surface fluxes.

721 We found the model validation exercise to be quite challenging. This is due to:
722 (i) unavoidable amplitude and displacement (spatial and temporal) errors associated with
723 mesoscale simulations; (ii) tremendous spatio-temporal variabilities of observed and mod-
724 eled SBL flow fields; and (iii) significant disagreement among the different observational
725 platforms. This last point was unexpected and needs further emphasis—in this work, we
726 found and reported on disagreements between: lidar and sounding (wind speed); scintil-
727 lometer and sonic anemometer (surface fluxes); lidar and sonic anemometer (variances).
728 Even two sonic anemometers located a few meters apart provided different data. In closing,
729 we note as Banta⁷ also did in highlighting distinctions distinctions between modelers and
730 their models/simulations on the one hand versus observations/data on the other: “everyone
731 believes a measurement except the person who took it,” but “no one believes a model result,
732 except the person who made it.” While such an innocuous statement is generally viewed
733 with some levity, in the context of SBL modeling, we advise modelers not to ‘believe’ based
734 on only one or two sets of observations, but rather validate their simulated results against
735 a diverse suite of observed datasets.

736 ACKNOWLEDGMENTS

737 We are grateful to all those researchers who painstakingly collected data during the
738 CASES-99 field campaign. The authors would like to thank Anantha Aiyyer, Robert Banta,
739 Bert Holtslag, Gary Lackmann, Larry Mahrt, Yelena Pichugina, and Jielun Sun for pro-
740 viding various types of observational data and/or for useful discussions. Computational

741 resources were generously provided by the Renaissance Computing Institute of Chapel Hill,
742 North Carolina. The authors acknowledge the financial support received from the National
743 Science Foundation (AGS-1122315, CBET-0967816, CBET-1050806) and the Air Force Of-
744 fice of Scientific Research (FA9550-12-1-0449). Any opinions, findings and conclusions or
745 recommendations expressed in this material are those of the authors and do not necessarily
746 reflect the views of the National Science Foundation or the Air Force Office of Scientific
747 Research.

748 REFERENCES

- 749 ¹W. C. Anderson, S. Basu, and C. W. Letchford. Comparison of dynamic subgrid-scale
750 models for simulations of neutrally buoyant shear-driven atmospheric boundary layer
751 flows. *Environ. Fluid Mech.*, 7:195–215, 2007.
- 752 ²E. L. Andreas. *Selected Papers on Turbulence in a Refractive Medium*. SPIE Milestone
753 Series, Vol. 25, Soc. Photo-Opt. Instr. Eng., Bellingham, WA, 1990.
- 754 ³A. Andrén. The structure of stably stratified atmospheric boundary layers: A large-eddy
755 simulation study. *Quart. J. Roy. Meteorol. Soc.*, 121:961–985, 1995.
- 756 ⁴S. P. Arya. *Introduction to Micrometeorology*. Academic Press, San Diego, CA, 2001. 420
757 pp.
- 758 ⁵Jong-Jin Baik, Seung-Bu Park, and Jae-Jin Kim. Urban flow and dispersion simulation
759 using a CFD model coupled to a mesoscale model. *Journal of Applied Meteorology and
760 Climatology*, 48(8):1667–1681, 2009.
- 761 ⁶R. M. Banta, R. K. Newsom, J. K. Lundquist, Y. L. Pichugina, R. L. Coulter,
762 and L. Mahrt. Nocturnal low-level jet characteristics over Kansas during CASES-99.
763 *Boundary-Layer Meteorol.*, 105:221–252, 2002.
- 764 ⁷Robert M Banta. High-resolution verification of mesoscale models using remote-sensing
765 measurements. In *5th International Symposium on Computational Wind Engineering
766 (CWE2010)*, 2010.
- 767 ⁸S. Basu and F. Porté-Agel. Large-eddy simulation of stably stratified atmospheric bound-
768 ary layer turbulence: a scale-dependent dynamic modeling approach. *J. Atmos. Sci.*, 63:
769 2074–2091, 2006.
- 770 ⁹S. Basu, E. Foufoula-Georgiou, and F. Porté-Agel. Synthetic turbulence, fractal inepo-

- 771 lation and large-eddy simulation. *Phys. Rev. E*, 70:026310, 2004.
- 772 ¹⁰S. Basu, F. Porté-Agel, E. Foufoula-Georgiou, J.-F. Vinuesa, and M. Pahlow. Revisiting
773 the local scaling hypothesis in stably stratified atmospheric boundary layer turbulence: an
774 integration of field and laboratory measurements with large-eddy simulations. *Boundary-*
775 *Layer Meteorol.*, 119:473–500, 2006.
- 776 ¹¹S. Basu, A. A. M. Holtslag, B. J. H. van de Wiel, A. F. Moene, and G.-J. Steeneveld.
777 An inconvenient “truth” about using sensible heat flux as a surface boundary condition
778 in models under stably stratified regimes. *Acta Geophysica*, 56:88–99, 2008.
- 779 ¹²S. Basu, J.-F. Vinuesa, and A. Swift. Dynamic LES modeling of a diurnal cycle. *J. Appl.*
780 *Meteorol. Climatol.*, 47:1156–1174, 2008.
- 781 ¹³S. Basu, A. A. M. Holtslag, and F. C. Bosveld. GABLS3 LES intercomparison study.
782 In *ECMWF/GABLS Workshop on “Diurnal cycles and the stable atmospheric boundary*
783 *layer”*, pages 75–82, ECMWF, 2011.
- 784 ¹⁴R. J. Beare, M. K. Macvean, A. A. M. Holtslag, J. Cuxart, I. Esau, J.-C. Golaz, M. A.
785 Jimenez, M. Khairoutdinov, B. Kosovic, D. Lewellen, T. S. Lund, J. K. Lundquist, A. Mc-
786 Cabe, A. F. Moene, Y. Noh, S. Raasch, and P. Sullivan. An intercomparison of large-eddy
787 simulations of the stable boundary layer. *Boundary-Layer Meteorol.*, 118:247–272, 2006.
- 788 ¹⁵RJ Beare, JM Edwards, and AJ Lapworth. Simulation of the observed evening transition
789 and nocturnal boundary layers: Large-eddy simulation. *Quarterly Journal of the Royal*
790 *Meteorological Society*, 132:81–99, 2006.
- 791 ¹⁶A. Beljaars. The parameterization of the planetary boundary layer. In *ECMWF Meteoro-*
792 *logical Training Course Lecture Series*, pages 1–57. 1992.
- 793 ¹⁷Zafer Boybeyi. A brief overview of mesoscale atmospheric features. In Zafer Boybeyi,
794 editor, *Mesoscale atmospheric dispersion*, pages 1–26. WIT Press, 2000.
- 795 ¹⁸Stuart Bradley. *Atmospheric acoustic remote sensing*. CRC Press, 271 pp., 2006.
- 796 ¹⁹R. A. Brost and J. C. Wyngaard. A model study of the stably stratified planetary
797 boundary layer. *J. Atmos. Sci.*, 35:1427–1440, 1978.
- 798 ²⁰M C Brower, editor. *Wind Resource Assessment: A Practical Guide to Developing a*
799 *Wind Project*. John Wiley & Sons Inc., 280 pp., 2012.
- 800 ²¹A. R. Brown, S. H. Derbyshire, and P. J. Mason. Large-eddy simulation of stable atmo-
801 spheric boundary layers with a revised stochastic subgrid model. *Quart. J. Roy. Meteorol.*
802 *Soc.*, 120:1485–1512, 1994.

- 803 ²²S. J. Caughey. Observed characteristics of the atmospheric boundary layer. In F. T. M.
804 Nieuwstadt and H. van Dop, editors, *Atmospheric Turbulence and Air Pollution Mod-*
805 *elling*, pages 107–158. D. Reidel Publishing Company, Dordrecht, 1982.
- 806 ²³Fei Chen and Jimy Dudhia. Coupling an advanced land surface-hydrology model with the
807 Penn State-NCAR MM5 modeling system. part i: Model implementation and sensitivity.
808 *Monthly Weather Review*, 129:569–585, 2001.
- 809 ²⁴Michael C Coniglio, Kimberly L Elmore, John S Kain, Steven J Weiss, Ming Xue, and
810 Morris L Weisman. Evaluation of wrf model output for severe weather forecasting from
811 the 2008 noaa hazardous weather testbed spring experiment. *Weather and Forecasting*,
812 25(2):408–427, 2010.
- 813 ²⁵J. Cuxart, A. A. M. Holtslag, and Coauthors. Single-column model intercomparison for
814 a stably stratified atmospheric boundary layer. *Boundary-Layer Meteorol.*, 118:273–303,
815 2006.
- 816 ²⁶H. A. R. de Bruin, W. M. L. Meijninger, A.-S. Smedman, and M. Magnusson. Displaced-
817 beam small aperture scintillometer test. Part I: the WINTeX data set. *Boundary-Layer*
818 *Meteorol.*, 105:129–148, 2002.
- 819 ²⁷James Done, Christopher A Davis, and Morris Weisman. The next generation of nwp:
820 Explicit forecasts of convection using the weather research and forecasting (wrf) model.
821 *Atmospheric Science Letters*, 5(6):110–117, 2004.
- 822 ²⁸Stefan Emeis. *Surface-based remote sensing of the atmospheric boundary layer*. Springer,
823 175 pp., 2010.
- 824 ²⁹T. Foken. *Micro-meteorology*. Springer, Berlin, Germany, 2008. 306 pp.
- 825 ³⁰K. J. Ha and L. Mahrt. Radiative and turbulent fluxes in the nocturnal boundary layer.
826 *Tellus A*, 55:317–327, 2003.
- 827 ³¹O. K. Hartogensis. *Exploring scintillometry in the stable atmospheric surface layer*. PhD
828 thesis, Wageningen University, The Netherlands, 2006.
- 829 ³²O. K. Hartogensis, H. A. R. de Bruin, and B. J. H. van de Wiel. Displaced-beam
830 small aperture scintillometer test. Part II: CASES-99 stable boundary-layer experiment.
831 *Boundary-Layer Meteorol.*, 105:149–176, 2002.
- 832 ³³R. J. Hill. Review of optical scintillation methods of measuring the refractive-index
833 spectrum, inner scale and the surface fluxes. *Wave. Random Media*, 2:179–201, 1992.
- 834 ³⁴A. A. M. Holtslag, G.-J. Steeneveld, and van de Wiel B. J. H. Role of land surface

- 835 temperature feedback on model performance for stable boundary layers. *Boundary-Layer*
836 *Meteorol.*, 125:361–376, 2007.
- 837 ³⁵S.-Y. Hong, Y. Noh, and J. Dudhia. A new vertical diffusion package with an explicit
838 treatment of entrainment processes. *Mon. Wea. Rev.*, 134:2318–2341, 2006.
- 839 ³⁶Song-You Hong. A new stable boundary-layer mixing scheme and its impact on the
840 simulated East Asian summer monsoon. *Quarterly Journal of the Royal Meteorological*
841 *Society*, 136:1481–1496, 2010.
- 842 ³⁷Song-You Hong, Jimy Dudhia, and Shu-Hua Chen. A revised approach to ice microphysi-
843 cal processes for the bulk parameterization of clouds and precipitation. *Monthly Weather*
844 *Review*, 132:103–120, 2004.
- 845 ³⁸Michael J Iacono, Jennifer S Delamere, Eli J Mlawer, Mark W Shephard, Shepard A
846 Clough, and William D Collins. Radiative forcing by long-lived greenhouse gases: Cal-
847 culations with the AER radiative transfer models. *Journal of Geophysical Research:*
848 *Atmospheres (1984–2012)*, 113(D13), 2008.
- 849 ³⁹M. A. Jiménez and J. Cuxart. Large-eddy simulations of the stable boundary layer using
850 the standard Kolmogorov theory: Range of applicability. *Boundary-Layer Meteorol.*, 115:
851 241–261, 2005.
- 852 ⁴⁰John S Kain. The Kain-Fritsch convective parameterization: an update. *Journal of*
853 *Applied Meteorology*, 43:170–181, 2004.
- 854 ⁴¹John S Kain and J Michael Fritsch. A one-dimensional entraining/detraining plume model
855 and its application in convective parameterization. *Journal of the Atmospheric Sciences*,
856 47(23):2784–2802, 1990.
- 857 ⁴²John S Kain, Steven J Weiss, Jason J Levit, Michael E Baldwin, and David R Bright.
858 Examination of convection-allowing configurations of the WRF model for the prediction
859 of severe convective weather: The SPC/NSSL Spring Program 2004. *Weather and fore-*
860 *casting*, 21(2):167–181, 2006.
- 861 ⁴³Albertson J. D. Chu C. R. Katul, G. G. and M. B. Parlange. Intermittency in atmospheric
862 surface layer turbulence: The orthonormal wavelet representation. In E Foufoula-Georgiou
863 and P Kumar, editors, *Wavelets in Geophysics*, pages 81–106. Academic Press, 1994.
- 864 ⁴⁴JT Kiehl, JJ Hack, GB Bonan, BA Boville, DL Williamson, and PJ Rasch. The national
865 center for atmospheric research community climate model: Ccm3. *J. Clim.*, 11(6):1131–
866 1149, 1998.

- 867 ⁴⁵B. Kosović and J. A. Curry. A large eddy simulation study of a quasi-steady, stably
868 stratified atmospheric boundary layer. *J. Atmos. Sci.*, 57:1052–1068, 2000.
- 869 ⁴⁶Vijayant Kumar, Gunilla Svensson, A A M Holtslag, Charles Meneveau, and Marc B
870 Parlange. Impact of surface flux formulations and geostrophic forcing on large-eddy sim-
871 ulations of diurnal atmospheric boundary layer flow. *Journal of Applied Meteorology and*
872 *Climatology*, 49(7):1496–1516, 2010.
- 873 ⁴⁷Y.-L. Lin. *Mesoscale dynamics*. Cambridge University Press, 630 pp., 2007.
- 874 ⁴⁸Erik Lindborg. Can the atmospheric kinetic energy spectrum be explained by two-
875 dimensional turbulence? *Journal of Fluid Mechanics*, 388:259–288, 1999.
- 876 ⁴⁹Y S Liu, S G Miao, C L Zhang, G X Cui, and Z S Zhang. Study on micro-atmospheric
877 environment by coupling large eddy simulation with mesoscale model. *Journal of Wind*
878 *Engineering and Industrial Aerodynamics*, 107-108:106–117, 2012.
- 879 ⁵⁰Yubao Liu, Alfred Bourgeois, Tom Warner, Scott Swerdlin, and Joshua Hacker. Imple-
880 mentation of observation-nudging based on FDDA into WRF for supporting ATEC test
881 operations. In *6th WRF Conference, NCAR, Boulder, CO*, 2006.
- 882 ⁵¹Yubao Liu, Tom Warner, Yuewei Liu, Claire Vincent, Wanli Wu, Bill Mahoney, Scott
883 Swerdlin, Keith Parks, and Jennifer Boehnert. Simultaneous nested modeling from the
884 synoptic scale to the LES scale for wind energy applications. *Journal of Wind Engineering*
885 *and Industrial Aerodynamics*, 99:308–319, 2011.
- 886 ⁵²Alex Mahalov and Mohamed Moustouai. Characterization of atmospheric optical turbu-
887 lence for laser propagation. *Laser & Photonics Reviews*, 4(1):144–159, 2010.
- 888 ⁵³L. Mahrt and D. Vickers. Contrasting vertical structures of nocturnal boundary layers.
889 *Boundary-Layer Meteorol.*, 105:351–363, 2002.
- 890 ⁵⁴P. J. Mason and S. H. Derbyshire. Large-eddy simulation of the stably-stratified atmo-
891 spheric boundary layer. *Boundary-Layer Meteorol.*, 53:117–162, 1990.
- 892 ⁵⁵W. M. L. Meijninger, O. K. Hartogensis, W. Kohsiek, J. C. B. Hoedjes, R. M. Zuur-
893 bier, and H. A. R. de Bruin. Determination of area-averaged sensible heat fluxes with a
894 large aperture scintillometer over a heterogeneous surface – Flevoland field experiment.
895 *Boundary-Layer Meteorol.*, 105:37–62, 2002.
- 896 ⁵⁶W. M. L. Meijninger, F. Beyrich, A. L’udi, W. Kohsiek, and H. A. R. de Bruin.
897 Scintillometer-based turbulent fluxes of sensible and latent heat over a heterogeneous
898 land surface – a contribution to LITFASS-2003. *Boundary-Layer Meteorol.*, 121:89–110,

- 899 2006.
- 900 ⁵⁷Jeffrey D Mirocha and Branko Kosović. A large-eddy simulation study of the influence
901 of subsidence on the stably stratified atmospheric boundary layer. *Boundary-layer mete-*
902 *orology*, 134:1–21, 2010.
- 903 ⁵⁸Eli J Mlawer, Steven J Taubman, Patrick D Brown, Michael J Iacono, and Shep-
904 ard A Clough. Radiative transfer for inhomogeneous atmospheres: RRTM, a validated
905 correlated-k model for the longwave. *Journal of geophysical research*, 102(D14):16663–16,
906 1997.
- 907 ⁵⁹Akashi Mochida, Satoru Iizuka, Yoshihide Tominaga, and Isaac Yu-Fat Lun. Up-scaling
908 CWE models to include mesoscale meteorological influences. *Journal of Wind Engineering*
909 *and Industrial Aerodynamics*, 99(4):187–198, 2011.
- 910 ⁶⁰CH Moeng, Jimy Dudhia, Joe Klemp, and Peter Sullivan. Examining two-way grid nesting
911 for large eddy simulation of the PBL using the WRF model. *Monthly weather review*, 135
912 (6):2295–2311, 2007.
- 913 ⁶¹Andreas Muschinski, Rod G Frehlich, and Ben B Balsley. Small-scale and large-scale
914 intermittency in the nocturnal boundary layer and the residual layer. *Journal of Fluid*
915 *Mechanics*, 515(1):319–351, 2004.
- 916 ⁶²F. T. M. Nieuwstadt. The turbulent structure of the stable, nocturnal boundary layer.
917 *J. Atmos. Sci.*, 41:2202–2216, 1984.
- 918 ⁶³F. T. M. Nieuwstadt. The turbulent structure of the stable, nocturnal boundary layer.
919 *J. Atmos. Sci.*, 41:2202–2216, 1984b.
- 920 ⁶⁴C G Nunalee and S Basu. Mesoscale modeling of coastal low-level jets: Implications for
921 offshore wind resource estimation. *Wind Energy*, 2013.
- 922 ⁶⁵J. J. O’Brien. A note on the vertical structure of the eddy exchange coefficient in the
923 planetary boundary layer. *J. Atmos. Sci.*, 27:1213–1215, 1970.
- 924 ⁶⁶Y. Ohya. Wind-tunnel study of atmospheric stable boundary layers over a rough surface.
925 *Boundary-Layer Meteorol.*, 98:57–82, 2001.
- 926 ⁶⁷Isidoro Orlanski. A rational subdivision of scales for atmospheric processes. *Bulletin of*
927 *the American Meteorological Society*, 56(5):527–530, 1975.
- 928 ⁶⁸J Park, S Basu, and L Manuel. Large-eddy simulation of stable boundary layer turbulence
929 and estimation of associated wind turbine loads. *Wind Energy*, 2013.
- 930 ⁶⁹Yelena L Pichugina, R M Banta, N D Kelley, B J Jonkman, S C Tucker, R K Newsom, and

- 931 W Alan Brewer. Horizontal-velocity and variance measurements in the stable boundary
932 layer using doppler lidar: Sensitivity to averaging procedures. *Journal of Atmospheric
933 and Oceanic Technology*, 25:1307–1327, 2008.
- 934 ⁷⁰Y.L. Pichugina and R.M. Banta. Stable boundary layer depth from high-resolution mea-
935 surements of the mean wind profile. *J. Appl. Meteorol. Climatol.*, 49(1):20–35, 2010.
- 936 ⁷¹G. S. Poulos and Coauthors. Cases-99: A comprehensive investigation of the stable
937 nocturnal boundary layer. *Bull. Amer. Meteorol. Soc.*, 83:555–581, 2002.
- 938 ⁷²D. O. ReVelle. Chaos and “bursting” in the planetary boundary layer. *J. App. Meteorol.*,
939 32:1169–1180, 1993.
- 940 ⁷³H Richardson, S Basu, and AAM Holtslag. Improving stable boundary-layer height es-
941 timation using a stability-dependent critical bulk Richardson number. *Boundary-Layer
942 Meteorology*, 2013. 10.1007/s10546-013-9812-3.
- 943 ⁷⁴Umberto Rizza, Mario M Miglietta, Otávio C Acevedo, Vagner Anabor, Gervasio A De-
944 grazia, Antonio G Goulart, and Hans R Zimmerman. Large-eddy simulation of the plan-
945 etary boundary layer under baroclinic conditions during daytime and sunset turbulence.
946 *Meteorological Applications*, 2012. DOI:10.1002/met.1284.
- 947 ⁷⁵E. M. Saiki, C.-H. Moeng, and P. P. Sullivan. Large-eddy simulation of the stably stratified
948 planetary boundary layer. *Boundary-Layer Meteorol.*, 95:1–30, 2000.
- 949 ⁷⁶K Heinke Schlünzen, David Grawe, Sylvia I Bohnenstengel, Ingo Schlüter, and Ralf Kopp-
950 mann. Joint modelling of obstacle induced and mesoscale changes—Current limits and
951 challenges. *Journal of Wind Engineering and Industrial Aerodynamics*, 99(4):217–225,
952 2011.
- 953 ⁷⁷Hyeyum Hailey Shin and Song-You Hong. Intercomparison of planetary boundary-layer
954 parametrizations in the WRF model for a single day from CASES-99. *Boundary-Layer
955 Meteorology*, 139(2):261–281, 2011.
- 956 ⁷⁸Chungwook Sim, Sukanta Basu, and Lance Manuel. On space-time resolution of inflow
957 representations for wind turbine loads analysis. *Energies*, 5:2071–2092, 2012.
- 958 ⁷⁹W. C. Skamarock, J. B. Klemp, J. Dudhia, D. O. Gill, D. M. Barker, W. Wang, and
959 J. G. Powers. A description of the advanced research wrf version 3. Technical Report
960 NCAR/TN-468+STR, National Center for Atmospheric Research, 2005.
- 961 ⁸⁰David R Stauffer and Nelson L Seaman. Use of four-dimensional data assimilation in
962 a limited-area mesoscale model. part i: Experiments with synoptic-scale data. *Monthly*

- 963 *Weather Review*, 118:1250–1277, 1990.
- 964 ⁸¹G. J. Steeneveld, B. J. H. van de Wiel, and A. A. M. Holtslag. Modeling the evolution of
965 the atmospheric boundary layer coupled to the land surface for three contrasting nights
966 in CASES-99. *J. Atmos. Sci.*, 63:920–935, 2005.
- 967 ⁸²G.-J. Steeneveld, J Vilà-Guerau de Arellano, A A M Holtslag, T Mauritsen, Gunilla
968 Svensson, and E I F de Bruijn. Evaluation of limited-area models for the representation
969 of the diurnal cycle and contrasting nights in CASES-99. *Journal of Applied Meteorology*
970 *and Climatology*, 47(3):869–887, 2008.
- 971 ⁸³GJ Steeneveld, BJH Van de Wiel, and AAM Holtslag. Diagnostic equations for the stable
972 boundary layer height: Evaluation and dimensional analysis. *J. Appl. Meteorol. Climatol.*,
973 46(2):212–225, 2007.
- 974 ⁸⁴D. J. Stensrud. *Parameterization schemes: Keys to understanding numerical weather*
975 *prediction models*. Cambridge University Press, 459 pp., 2007.
- 976 ⁸⁵B. Storm and S. Basu. The WRF model forecast-derived low-level wind shear climatology
977 over the United States Great Plains. *Energies*, 3:258–276, 2010.
- 978 ⁸⁶B. Storm, J. Dudhia, S. Basu, A. Swift, and I. Giammanco. Evaluation of the Weather Re-
979 search and Forecasting model on forecasting low-level jets: Implications for wind energy.
980 *Wind Energy*, 12:DOI: 10.1002/we.288, 2008.
- 981 ⁸⁷R. B. Stull. *An Introduction to Boundary Layer Meteorology*. Kluwer Academic Publish-
982 ers, Dordrecht, The Netherlands, 1988. 670 pp.
- 983 ⁸⁸J. Sun, D. H. Lenschow, S. P. Burns, R. M. Banta, R. Coulter, S. Frasier, T. Ince,
984 C. Nappo, L. Mahrt, D. Miller, and B. Skelly. Atmospheric disturbances that generate
985 intermittent turbulence in nocturnal boundary layers. *Boundary-Layer Meteorol.*, 110:
986 255–279, 2004.
- 987 ⁸⁹Gunilla Svensson, A A M Holtslag, V Kumar, T Mauritsen, G J Steeneveld, W M
988 Angevine, E Bazile, A Beljaars, E I F de Bruijn, A Cheng, L Conangla, J Cuxart, M Ek,
989 M J Falk, F Freedman, H Kitagawa, V E Larson, A Lock, J Mailhot, V Masson, S Park,
990 J Pleim, S Söderberg, W Weng, and M Zampieri. Evaluation of the diurnal cycle in the
991 atmospheric boundary layer over land as represented by a variety of single-column models:
992 the second gabl experiment. *Boundary-Layer Meteorology*, 140(2):177–206, 2011.
- 993 ⁹⁰Charles Talbot, Elie Bou-Zeid, and Jim Smith. Nested mesoscale-large eddy simulations
994 with WRF: Performance in real test cases. *Journal of Hydrometeorology*, 13:1421–1441,

995 2012.

996 ⁹¹I. Troen and L. Mahrt. A simple model of the atmospheric boundary layer: sensitivity to
997 surface evaporation. *Boundary-Layer Meteorol.*, 37:129–148, 1986.

998 ⁹²B. van de Wiel. *Intermittent Turbulence and Oscillations in the Stable Boundary Layer*
999 *over Land*. PhD thesis, Wageningen University, Netherlands, 2002.

1000 ⁹³B. J. H van de Wiel, A. F. Moene, G.-J. Steeneveld, P Baas, F. C Bosveld, and A. A. M
1001 Holtslag. A conceptual view on inertial oscillations and nocturnal low-level jets. *Journal*
1002 *of the Atmospheric Sciences*, 67:2679–2689, 2010.

1003 ⁹⁴BJH van de Wiel, A. F. Moene, O. K. Hartogensis, H. A. R De Bruin, and A. A. M
1004 Holtslag. Intermittent turbulence in the stable boundary layer over land. Part III: A
1005 classification for observations during cases-99. *J. Atmos. Sci.*, 60:2509–2522, 2003.

1006 ⁹⁵D. Vickers and L. Mahrt. Quality control and flux sampling problems for tower and
1007 aircraft data. *J. Atmos. Oceanic Technol.*, 14:512–526, 1997.

1008 ⁹⁶D. Vickers and L. Mahrt. Evaluating formulations of stable boundary layer height. *J.*
1009 *Appl. Meteorol.*, 43:1736–1749, 2004.

1010 ⁹⁷John C Wyngaard. Toward numerical modeling in the “terra incognita”. *Journal of the*
1011 *atmospheric sciences*, 61(14):1816–1826, 2004.

1012 ⁹⁸Tetsuji Yamada and Katsuyuki Koike. Downscaling mesoscale meteorological models for
1013 computational wind engineering applications. *Journal of Wind Engineering and Industrial*
1014 *Aerodynamics*, 99(4):199–216, 2011.

1015 ⁹⁹Frank J Zajackowski, Sue Ellen Haupt, and Kerrie J Schmehl. A preliminary study of
1016 assimilating numerical weather prediction data into computational fluid dynamics models
1017 for wind prediction. *Journal of Wind Engineering and Industrial Aerodynamics*, 99(4):
1018 320–329, 2011.

1019 ¹⁰⁰Shiyuan Zhong and Jerome Fast. An evaluation of the MM5, RAMS, and Meso-Eta
1020 models at subkilometer resolution using VTMX field campaign data in the Salt Lake
1021 Valley. *Monthly Weather Review*, 131(7):1301–1322, 2003.

1022 ¹⁰¹Bowen Zhou and Fotini Katopodes Chow. Large-eddy simulation of the stable boundary
1023 layer with explicit filtering and reconstruction turbulence modeling. *J. Atmos. Sci.*, 68:
1024 2142–2155, 2011.